PROTOTYPE DEVELOPMENT OF A LIGHT SPORT AIRCRAFT SWITCHED RELUCTANCE MOTOR

PROTOTYPE DEVELOPMENT OF A LIGHT SPORT AIRCRAFT SWITCHED RELUCTANCE ELECTRIC MOTOR

By

Sanjeev Ravichandran, MASc.

A Dissertation

Submitted to the School of Graduate Studies

in Partial Fulfillment of the Requirements

for the Degree Master of Applied Sciences

Master of Applied Science (2025) McMaster University

(Mechanical Engineering) Hamilton, Ontario, Canada

TITLE: Prototype Development of a Light Sport Aircraft Switched Reluctance Electric Motor

AUTHOR: Sanjeev Ravichandran

B.Tech. School of Mechanical Engineering

(Manipal Academy of Higher Education, Dubai)

SUPERVISOR: Dr. Stephen C. Veldhuis, Professor and Director (MMRI)

Ph.D. (McMaster University)

Dr. Berker Bilgin, Assistant Professor

Ph.D. (Illinois Institute of Technology)

NUMBER OF PAGES: 126

Abstract

The increasing global emphasis on reducing greenhouse gas emissions has amplified interest in the electrification of light sport aircraft, particularly for training and recreational purposes. A Switched Reluctance Motor (SRM) is a groundbreaking technology in this field, offering a cost-effective, robust, and efficient alternative to permanent magnet motors. Its straightforward design and ability to perform reliably in elevated temperatures and high-speed make it suitable for aviation applications. While there are challenges surrounding the manufacturing and assembly of SRMs, their strengths position them as a strong contender in the market. The prototype development presented in this thesis focuses primarily on the mechanical design, manufacturing, and assembly of an SRM with a stator outer diameter of 280 mm and a relatively small airgap length of 0.4 mm airgap length between rotor and stator. The proposed SRM is designed to be a direct replacement for a 70 kW Permanent Magnet Synchronous Motor (PMSM) to meet the stringent volume restrictions and operational requirements specific to an aerospace application. This research investigates manufacturing techniques of motor components, precision assembly of rotor and stator cores. Challenges including dimensional accuracy, thermal management, and proper motor component assembly are also discussed. Maintaining mechanical alignment and a small air gap is critical and essential to the motor's efficiency and functionality. This work presents the SRM as an alternative for the

electrification of light sport aircraft, contributing to more sustainable aviation solutions.

Acknowledgement

First, I would like to express my deepest gratitude to Supervisors, Dr. Stephen Veldhuis and Dr. Berker Bilgin, for their invaluable guidance, continuous support, and motivation throughout my research. Their insights and expertise were instrumental in helping me navigate through the complexities of this project.

I would also like to extend my sincere thanks to the members of the Mechanical Engineering Department at McMaster University for their constructive feedback and for fostering a collaborative and encouraging environment. Special thanks to Dr. Sumanth Shankar for the helpful discussions and assistance in overcoming the technical challenges faced during this research.

My heartfelt thanks go to McMaster Manufacturing Research Institute (MMRI) and McMaster Automotive Resource Centre, (MARC) for providing access to the necessary equipment, materials, and facilities for the manufacturing and assembly of the prototype.

I would like to express my deepest appreciation to my parents, Mr. Ravichandran and Mrs. Meenakshi, for their unwavering support, encouragement, and belief in me. Their sacrifices and guidance have been the foundation of my success.

Finally, I would like to thank whomever contributed to the completion of this thesis in ways big and small. Thank you all for your contributions and support.

Contents

List of Figures

List of Tables

Notations

Abbreviations-

SRM	Switched Reluctance Motor
AWG	American Wire Gauge
LSA	Light sport Aircraft
CTE	Coefficient of Thermal Expansion
PM	Permanent Magnet
IM	Induction Motor
PMSM	Permanent Magnet Synchronous Motor
WEG	Water Ethylene Glycol
CMM	Coordinate Measuring Machine
LMC	Least Material Condition
PI	Polarization Index
HIPOT	High Potential Test
SLS	Selective Laser Sintering
CAD	Computer aided design
FEA	Finite Element Analysis

GHG	Greenhouse gases
CNC	Computerised Numerical Control
FAA	Federal Aviation Administrator
ICE	Internal Combustion Engine
EASA	European Union Aviation Safety Agency
AFPMSM	Axial Flux Permanent Magnet Synchronous Motors

Symbols and Units

°C	Degrees Celsius
A	Ampere
V	Voltage
W	Watts
G/CC	Grams Per Cubic Centimetre
MPa	Megapascal
Nm	Newton-metre
Δ	Delta
Psi	Pound-force per square inch

Ω	Ohm
W/(m·K)	Watts per Metre - Kelvin
Lpm	Litres per minute
RPM	Rotations Per Minute
kg	Kilogram
OZ.	Ounces
Lbs	Pounds

Chapter 1 Introduction

Concerns about global warming have been the primary reason for the notable acceleration of the push for transportation electrification over the last ten years. If demand trends continue, the aviation industry, which contributes between 2% to 5% of global greenhouse gas emissions yearly, is expected to increase emissions by 2050 significantly [1][2][3]. Due to current battery technology limitations, which limit the energy density and the range of electric aircraft, the aviation industry has progressed more slowly to electrify than other transportation sectors. Electrifying aviation is still the most practical way to reduce aircraft emissions, aside from using expensive alternatives like sustainable aviation biofuels [4].

Electrification in aviation can reduce emissions through several approaches including substituting standard non-propulsive systems, such as hydraulic or pneumatic, with electrically powered systems (a concept known as more electric aircraft); adopting hybrid-electric propulsion systems; or fully transitioning to all-electric aircraft powered solely by electric motors. Each of these approaches requires electric motors that are efficient, reliable, and highly robust. The robustness, low manufacturing costs, and alternative from permanent magnets make SRMs appealing, and thus, ideal for propelling electrification in the aviation sector [7].

1.1 Motivation

Global warming concerns are driving the electrified aircraft market, which is expected to grow to $178 billion by 2040. That represents a significant increase over the market's $99 million size in 2018 [5]. The energy density of batteries restricts the range of electric aircraft. Improvements in power trains and energy storage technologies significantly impact an aircraft's range. Long-haul flights may not be possible with the current energy storage system technology. Business aviation, air taxis, training aircraft, and recreational sport aircraft are short-haul flights not intended for long distances and can be electrified even with the current technology [6].

The next generation of long-haul aircraft with large payload and passenger capacities can benefit from the research and development done on electrified short-haul aircraft. One of the best options for the aviation propulsion system is an SRM. An SRM's phases are electrically isolated from one another. This makes an SRM a fault-tolerant motor technology. SRM is appropriate for high-speed and high-temperature operation due to its straightforward and robust design, which does not include permanent magnets or conductors on the rotor. Since a propeller produces much more noise and the pilot cabin is typically isolated from the drivetrain, the conventional disadvantages of SRMs, such as torque ripples and acoustic noise, are not a significant issue for these propulsion systems. A major advantage is that SRMs are not impacted by the

fluctuating price of rare earth materials because they do not require permanent magnets [7].

1.2 Contribution

The development focuses on creating a prototype of an SRM for light sport aircraft propulsion. To enhance torque density, HIPERCO® 50A high magnetic saturation iron-cobalt alloy from Carpenter Technology – is chosen as the SRM's core magnetic material. The research explores manufacturing techniques and precise rotor and stator assembly, addressing dimensional accuracy, thermal management, and component integration challenges. Attention is given to ensuring mechanical alignment and maintaining a small air gap, both crucial to the motor's operational efficiency. Precision lamination of rotor and stator cores, which is required for consistent magnetic performance, presents significant challenges. Coil winding presents additional challenges, necessitating careful handling to avoid insulation damage, maintaining winding tension, and ensure uniformity. Stator encapsulation is used to increase reliability by providing enhanced thermal stability and environmental protection, both critical in aviation applications. Post-assembly testing, which includes coolant pressure, Hi-pot, and surge tests for the encapsulated stator, confirms suitability of the prototype for a operational requirement of the motor.

1.3 Outline of thesis

Chapter 1: Introduction

This chapter discusses the need for cleaner and more efficient propulsion technologies, particularly in the aviation sector, which produces significant greenhouse gas emissions. It discusses the potential for electrifying light sport aircraft with an SRM instead of permanent magnet synchronous motors. The motivation for creating an SRM prototype that adheres to aerospace constraints is presented alongside the thesis' structure and intended contributions to the field.

Chapter 2: Overview of Electric Motors for Aircraft Applications

This chapter overviews the current electric motor technologies used in aircraft applications, focusing on light sport aircraft. It discusses the fundamental principles and benefits of various motor types, particularly SRMs, and their potential for aviation electrification. The key challenges, constraints, and operational principles of motors in aviation settings are also discussed, laying the groundwork for SRM's unique advantages and limitations.

Chapter 3: Mechanical Design of an LSA SRM

This chapter discusses the design process of an LSA SRM, beginning with CAD modelling of its components and progressing to the design considerations and specifications required for optimal performance. It emphasizes the importance of finite element analysis (FEA) in evaluating electromagnetic and thermal behaviour,

advanced design techniques, and manufacturing challenges encountered during SRM production.

Chapter 4: Manufacturing of the SRM Components

This chapter explores the methods utilized in manufacturing the housing, stator, rotor, and shaft, as well as the sourcing and material selection processes for SRM components. It assesses the manufacturing process's outcomes and thoroughly examines manufacturing difficulties like accuracy and dimensional tolerances. The success of the manufacturing process is also assessed by presenting dimensional accuracy and inspection techniques, such as the use of a Coordinate Measuring Machine (CMM).

Chapter 5: Assembly of the LSA SRM and Functional Validation of the Assembly Components

The steps in assembling the SRM prototype include interference press fitting, rotor balancing, and thermal expansion calculations. This chapter outlines several testing methods, such as stator encapsulation, coil phase resistance testing, and coolant leak and flow rate tests. High-potential testing is also carried out to guarantee the stator windings' insulation integrity, confirm no breakdown under high voltage conditions, and assess the challenges involved in stator building. Surge test is also used to validate that there were no issues with the integrity of the stator coil, such as shorted turns.

Chapter 6: Conclusions and Future Work

This chapter concludes the development of the prototype, summarizing key achievements and challenges. It also outlines potential future improvements and research directions for enhancing the motor's design and performance.

Chapter 2 - Overview of Electric Motors for Aircraft Applications

2.1 Introduction

Currently, consumer electric vehicles are the focus of transportation, while commercial electric vehicles are entering the market rapidly. Reducing greenhouse gas (GHG) emissions, operating costs, and reliance on fossil fuels is the main driver behind the push for mass electrification. According to the Environmental and Energy Study Institute, commercial aviation accounted for 2.4% of global greenhouse gas emissions in 2018; by 2050, that percentage is predicted to triple [8]. Ideally, the way to minimize aviation's carbon footprint is through fully electric aircraft. However, because current aviation capabilities are limited by batteries and energy density, significant advancements are required before industry can achieve full electrification. As shown in *Figure 1,* the aircraft's weight is crucial because aviation requires lift force. Even though the best commercially available batteries today have a much lower energy density than aviation fuel, research is still being done on alternative energy storage options like hydrogen fuel cells [7].

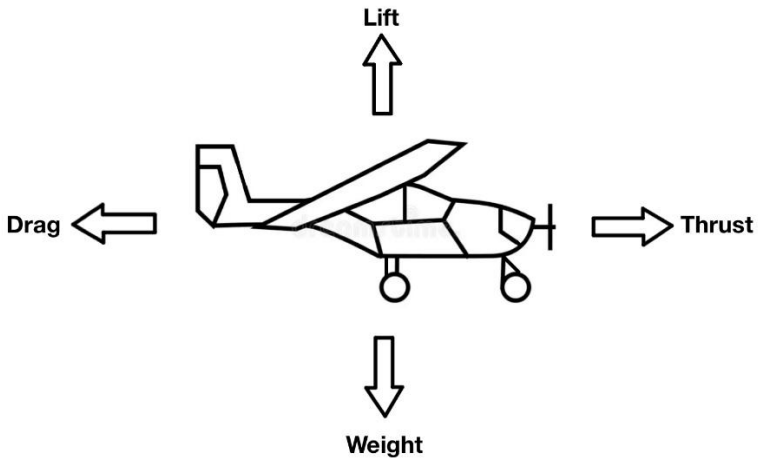

Figure 1 - Aircraft Forces

Despite weight issues, some applications, especially Light Sport Aircraft (LSA) can be electrified using current battery technologies due to the trade-off between weight and range. With expected uses in flight schools and recreational aviation, the LSA industry has been electrifying recently. Electric LSAs are anticipated to become more prevalent, and the progress made in this area may eventually expand, influencing future developments in commercial aviation.

2.2 Existing Electric Motor Types

Induction and permanent magnet motors are the most common motor drive systems used in transportation, commercial, residential, and industrial settings. The typical structure of these motors is depicted in *Figure 2*, along with a comparison to an SRM. This is where SRM's most significant benefit shows itself. These motors are made up of a rotor, windings, and stator. However, SRM lacks one item compared to induction

motors and permanent magnet motors. Magnets are inserted into the rotor of a permanent magnet motor to provide rotor excitation, as shown in *Figure 2 (a)*. An induction motor uses rotor bars to achieve magnetic induction and generate forces on the rotor, as shown in *Figure 2 (b)*. An SRM uses ferromagnetic material as the core to achieve magnetic induction as shown in *Figure 2 (c)* [9].

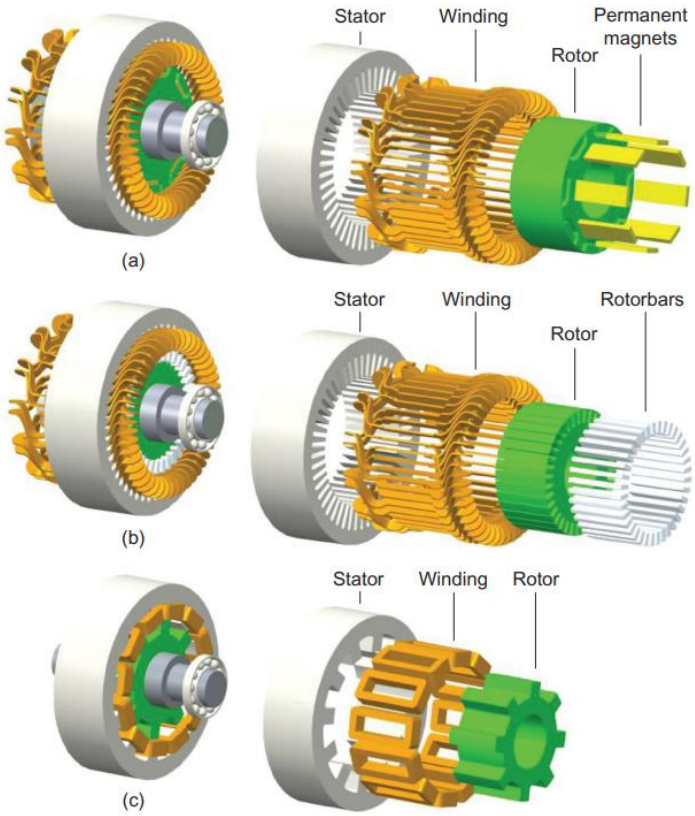

Figure 2 - Types of structure of electric machines (a) PMSM (b) IM (c) SRM [9]

2.2.1 Permanent Magnet Motor

Permanent Magnet Synchronous Motors (PMSMs) are well-known for their high efficiency and torque density, particularly in applications such as electric vehicles and

home appliances. PMSMs generate a strong magnetic field by incorporating magnets into the rotor, which contributes to their smooth and efficient operation, especially at low speeds. This magnetic field can be adjusted by carefully positioning the magnets to optimize the motor's performance. As a result, PMSMs are commonly used in applications that require reliability and efficiency in small spaces. However, Permanent Magnets (PMs) are made from rare-earth materials such as neodymium and dysprosium, which are expensive and have supply chain issues. These materials are temperature sensitive; elevated temperatures can significantly reduce their performance. This sensitivity poses a threat for industries seeking long-term, sustainable solutions, particularly given the world's reliance on a few major suppliers of rare-earth minerals, primarily China [9].

2.2.2 Induction Motor

Induction Motors (IMs) dominate several industrial, commercial, and residential applications because of their affordable price and mature technology. IMs generate torque by creating a magnetic field in the rotor that interacts with the stator's magnetic field. There are two primary varieties: squirrel-cage IMs, which generally incorporate due-casted aluminum bars on the rotor, and wound-rotor IMs, which use three-phase windings on the rotor. The primary advantage of induction machines is their self-starting capability, allowing them to operate without a power converters or position sensor. IMs have been widely used for decades due to their simplicity. Their reliance on rotor currents can result in significant energy losses, especially in high-

torque applications, and they have lower efficiency and power factor than PM motors [9].

2.2.3 Switched Reluctance Motor

Recently, SRMs have drawn attention due to their straightforward design that does not require rotor conductors and permanent magnets found in other motor types. The simple construction of SRMs make them easier to manufacture, which lowers costs and increases durability when the motor operates in high-temperature or high-speed conditions. Thus, SRMs are desired by the robust and effective motor solutions industries. However, SRMs can have high torque ripple, vibration, and noise level. Despite these challenges, SRMs' robustness, affordability, and high-speed performance make them increasingly valuable as industries search for environmentally friendly substitutes for intricate motor designs [9].

2.3 Operating Principles of Switched Reluctance Motors (SRM)

SRMs produce rotational motion using the magnetic reluctance principle. They have a salient-pole construction on the stator and rotor, which gives SRMs unique operating characteristics. An SRM rotor is typically a ferromagnetic material without windings, conductors, or permanent magnets. This simple rotor structure reduces production complexity. The stator, made of a ferromagnetic material, has windings on each pole as shown in *Figure 3*. These windings are energized in a specific order to generate magnetic field that interact with the rotor, resulting in torque acting on the rotor.

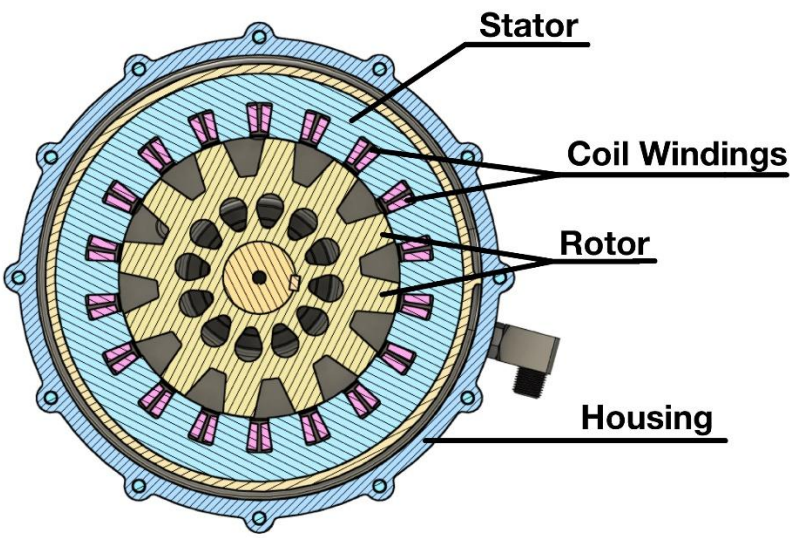

Figure 3 – Cross-section view of an SRM

When a stator pole is energized, it generates an electromagnetic field that attracts the nearest rotor pole, reducing magnetic reluctance between them. When the rotor aligns with the stator pole, the magnetic circuit achieves minimum reluctance, completing one step in the rotational movement. The process is repeated as different stator poles are energized sequentially, resulting in continuous rotation [9].

The torque production in an SRM is based on change in the reluctance of the magnetic circuit with rotor position. The torque in each phase of an SRM is determined by the rotor and stator poles' relative positions and the excitation current in the stator windings. Unlike typical motors, SRMs do not use direct rotor excitation, such as permanent magnets or induced currents. This feature allows SRMs to work efficiently at high speeds and over a wide range of temperatures.

2.3.1 Advantages of a Switched Reluctance Motor

SRM stands out for its simplicity and several advantages over other motor types, making it ideal for modern applications. SRMs are cost-effective because they do not require rare-earth materials. Instead, they rely on widely available copper and steel. Their robust design, which includes a rotor free of windings and magnets, increases durability and makes them ideal for high-speed and harsh environments, potentially resulting in a longer lifespan under stress. They are also highly fault-tolerant, with each phase electrically isolated. This enables torque generation even if one phase fails. Furthermore, SRMs contribute to sustainability by reducing reliance on rare-earth materials, which are expensive, environmentally challenging to source, and subject to supply chain volatility, providing a resource-secure alternative for industries transitioning to sustainable motor solutions.

2.3.2 Challenges with a Switched Reluctance Motor

SRMs have a cost-effective design, but they can have several challenges that must be overcome to improve their performance in practical applications. Torque ripples are a significant issue caused by the inherent reluctance-based torque generation in SRMs. Torque ripple may occur due to variations in the generated torque across each phase transition. The primary source of noise and vibration in an SRM is not the torque ripple but the radial forces acting on the stator. These radial forces result from the motor's salient-pole structure and the magnetic interactions during operation.

Addressing these challenges requires an optimum stator and rotor geometry, frame, and current control design. Due to SRMs' nonlinear magnetic properties, a relatively complex control is necessary that involves advanced control algorithms and specifically constructed power electronic circuits to handle unipolar currents. Managing these nonlinear properties is critical for obtaining the desired performance. Control technology (advanced systems, methods and algorithms) and modelling advances have made these difficulties more manageable.

2.4 Existing Electric Motors for Light Sport Aircraft

Many companies, including startups and established corporations, are investigating the prospect of electrifying LSA. Improved control over acceleration and power output allows the aircraft to fly quicker and more efficiently. *Figure 4* shows the *Spirit of Innovation*, Rolls-Royce's next all-electric light sport aircraft. It is claimed to be one of the fastest all-electric aircraft in the world. The airplane has three world records:

- Maximum speed of 555.2 km/h over three km
- Maximum speed of 532.7 km/h over fifteen km
- 3 kilometers climbed in 202 seconds

Three motors are assembled in a stack to generate an immense amount of power. They are produced in collaboration with the automobile powertrain provider YASA. The powertrain generates 400 kW and operates at 2200 rpm [7].

Figure 4 - Rolls-Royce's record-breaking Spirit of Innovation electric aircraft [10]

An aircraft engine must be approved before it may be used in aviation. Due to safety requirements, the certification process in the aviation sector is rigorous and stringent, particularly avoiding malfunctioning at a high altitude while flying. The Federal Aviation Administrator (FAA) oversees approving Internal Combustion Engine (ICE) aircraft in the United States and issues several guidelines. The electrified LSA is airworthy according to standard certification; nevertheless, the motor, controller, and battery require additional consideration for accreditation. The European Union Aviation Safety Agency (EASA) certifies aircraft and pilots throughout Europe. The EASA motor certification is transparent, and Pipistrel has published its certification for an electric LSA motor, the 13 E-881, on its website. According to EASA, Reg. (EU) 2018/1139 Article 77 (1) and Commission Reg. (EU) No.748/2012 should be considered when designing electrical motors for electric aircraft [7].

Recently, electric motors with improved power density and efficiency have been designed for airplane propulsion. *Table 1* outlines those for which operational data is publicly available .

Table 1 - Motor Specification from Pipistrel, Siemens and Magnix for light sport aircraft [7]

Motor Name		SP70D	SP55D	SP260D	E-811	MAGNI500	MAGNI250
Company		Siemens	Siemens	Siemens	Pipistrel	Magnix	Magnix
$P_{Continous}$		70kW @2600 rpm	55kW @3000 rpm	260 kW @2500 rpm	49.2 kW @2350 rpm	560 kW	280 kW
P_{Max}		92kW up to 2 min	72kW up to 2 min		57.6 kW up to 90 secs		
ω_{cont}		2600 rpm	3000 rpm		2350 rpm	1900 rpm	1900 rpm
ω_{max}		2600 rpm	3000 rpm		2500 rpm	2600 rpm	3000 rpm
T_{cont}		260 Nm	180 Nm	1000 Nm	200 Nm	2814 rpm	1407 Nm
T_{max}		340 Nm	240 Nm		220 Nm		
V_{dc}		350-450 V	350-450 V	580 V	400 V	450-750 V (V_n=540)	490-750 V (V_n=540)
m_{total}		26 kg	26 kg	50 kg	22.7 kg	135 kg	71 kg
Cooling		Water / Glycol	Water / Glycol	Oil @ 90°C	Water / Glycol	Liquid Cooling	Liquid Cooling
Efficiency		Max. 95%		Max. 95%		> 93%	> 93%
Size	Length			30 cm	9.1 cm	55.8 cm	27.9 cm
	Diameter			41.8 cm	26.8 cm	65.2 cm	55.9 cm
Fault Protection				Redundant 3-Ø windings		4 x 3-Ø Architecture	2 x 3-Ø Architecture
Other Details		Direct drive for Max. Power density			Axial flux sync. PM	No Gearbox needed, High torque at low speed	

Several companies, such as Rolls-Royce, and Pipistrel, have made substantial progress in designing electric motors specifically for LSA applications. Their designs are engineered to fulfill the aviation industry's stringent requirements, including advanced motor design, new winding processes, improved cooling systems, and

specific transmission designs. MagniX relies on permanent magnet synchronous motors (PMSMs) to deliver consistent power [11]. Pipistrel uses axial flux permanent magnet synchronous motors (AFPMSMs) to produce a compact design that shortens the motor's axial length, resulting in an efficient and lightweight system [12]. Siemens has launched high-power density PMSM systems in multiple configurations, including simple, efficient gearboxes and direct-drive systems, which reduce complexity and improve reliability [13].

The Siemens SP70D is a permanent magnet motor designed for electric aviation applications. It works particularly well with direct-drive propellers and has been tested on Bye Aerospace's eFlyer light sport aircraft. An initial prototype SRM is intended to serve as proof of concept, demonstrating that SRMs can meet the torque, speed, volume, and efficiency requirements of the original SP70D.

The SP70D is designed for direct-drive propeller applications on one or two-seater aircraft. As a result, it is a low-speed, high-torque motor with peak power requirements slightly lower than 100 kW. The SP70D parameters are provided in *Table 2* [14].

Table 2 - Specification of Siemens SP70D

1	Maximum Power (120s)	92 kW
2	Continuous Power	70 KW
3	Maximum Speed	2600 RPM
4	Maximum Torque	340 Nm
5	Continuous Torque	260 Nm
6	Bus Voltage	350-450 VDC
7	Mass	26 kg
8	Cooling	Water Ethylene Glycol (WEG)
9	Stack Length (Est.)	50-100 mm
10	Motor Diameter (Est.)	300 mm
11	Shaft Diameter (Est.)	50 mm

The primary heat extraction method is a water jacket around the stator's outer diameter. Coolant WEG's poor dielectric properties make it unsuitable for direct cooling within the motor. Some forced air cooling can be achieved by channelling airflow over the motor housing, leveraging the airflow that naturally flows through the fuselage. This dual cooling approach, which combines water and air cooling, was successfully demonstrated in the Magnus eFusion electric aircraft, showing how both methods can work together to manage heat in an electric motor in an aviation atmosphere [12].

2.5 Summary

Compared to traditional LSAs, electrified LSAs are more efficient and feature smaller motors, better aerodynamics, a more straightforward gearbox, and efficient cooling systems. It overviews various motor types, including permanent magnet, induction, and switched reluctance motor (SRM). The operating principles of SRM are discussed, highlighting their unique advantages, such as robustness and cost-effectiveness, as well as challenges like noise and vibration. Additionally, it examines motors' specific requirements and constraints in aviation environments. It discusses existing electric motors used in light sport aircraft, including the Siemens SP70D motor, a benchmark for this prototype, which decided the design's specifications, manufacturing feasibility, and assembly method of the LSA SRM.

Chapter 3: Mechanical Design of the LSA SRM

The primary motor dimensions of the LSA SRM are 350 mm in diameter and 250 mm in length, as shown in *Figure 5,* excluding the shaft and encoder. The stator core measures 280 mm in diameter and 100 mm in axial length, like the SP70D model.

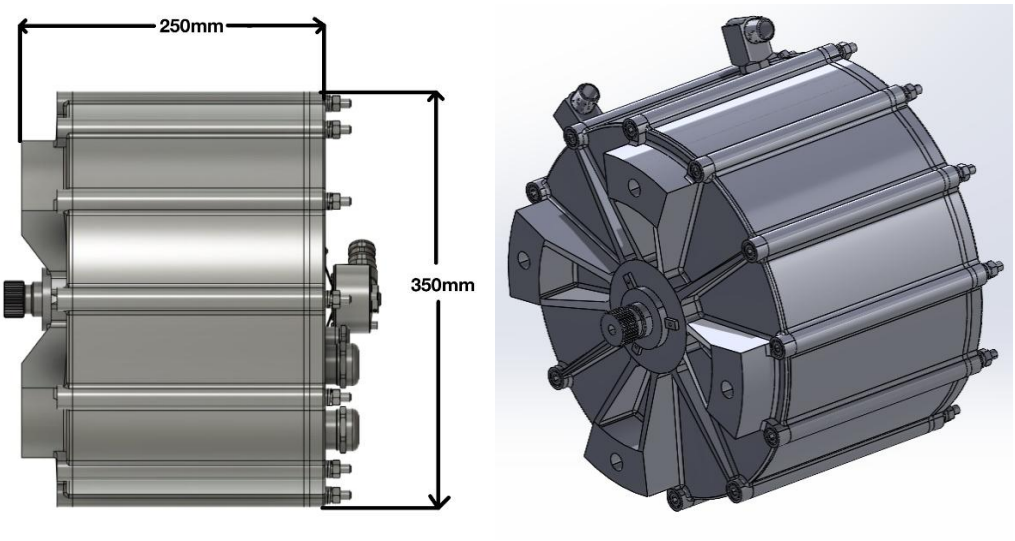

Figure 5 - LSA SRM Motor Dimension

Between the rotor and stator, a 0.4 mm air gap is maintained as shown in *Figure 6.*

This is relatively smaller than what is typically found in permanent magnet machines of comparable size, where air gaps range from 0.6 mm to 1.0 mm. However, this gap aligns with industry standards for commercially available SRMs. The rotor also features a 50 mm bore to accommodate a press-fit hardened steel shaft, which extends

to a total length of 318 mm, allowing additional room for an encoder attachment at the non-driving end of the shaft.

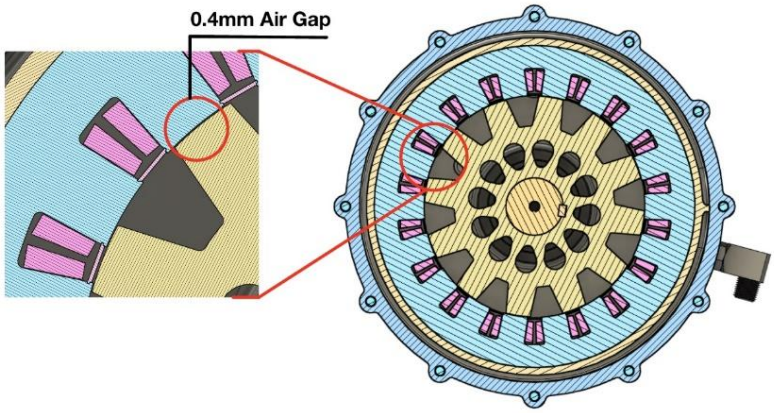

Figure 6 - Airgap between stator and rotor

3.1 Structural Design of the LSA SRM

The housing and drive shaft are the motor parts that are usually seen from outside. The housing serves as the primary structure and supports numerous other components that can only be seen if the housing is opened. *Figure 7* shows the major components of the LSA SRM in an exploded view. The flowchart in *Figure 8* shows project flow and the three significant subassemblies of the LSA SRM: the stator subassembly, the rotor Subassembly, and the housing subassembly.

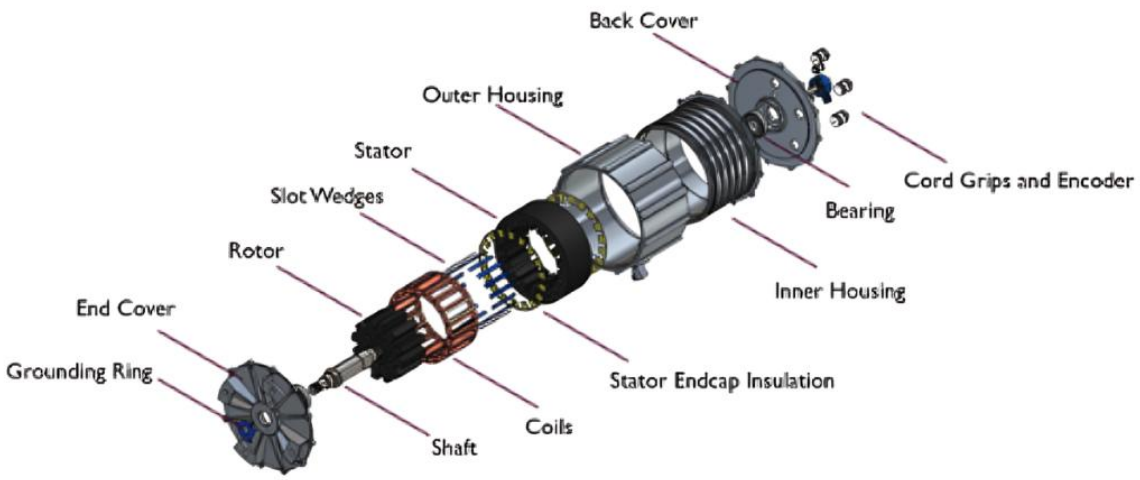

Figure 7 - Exploded View of LSA SRM Design

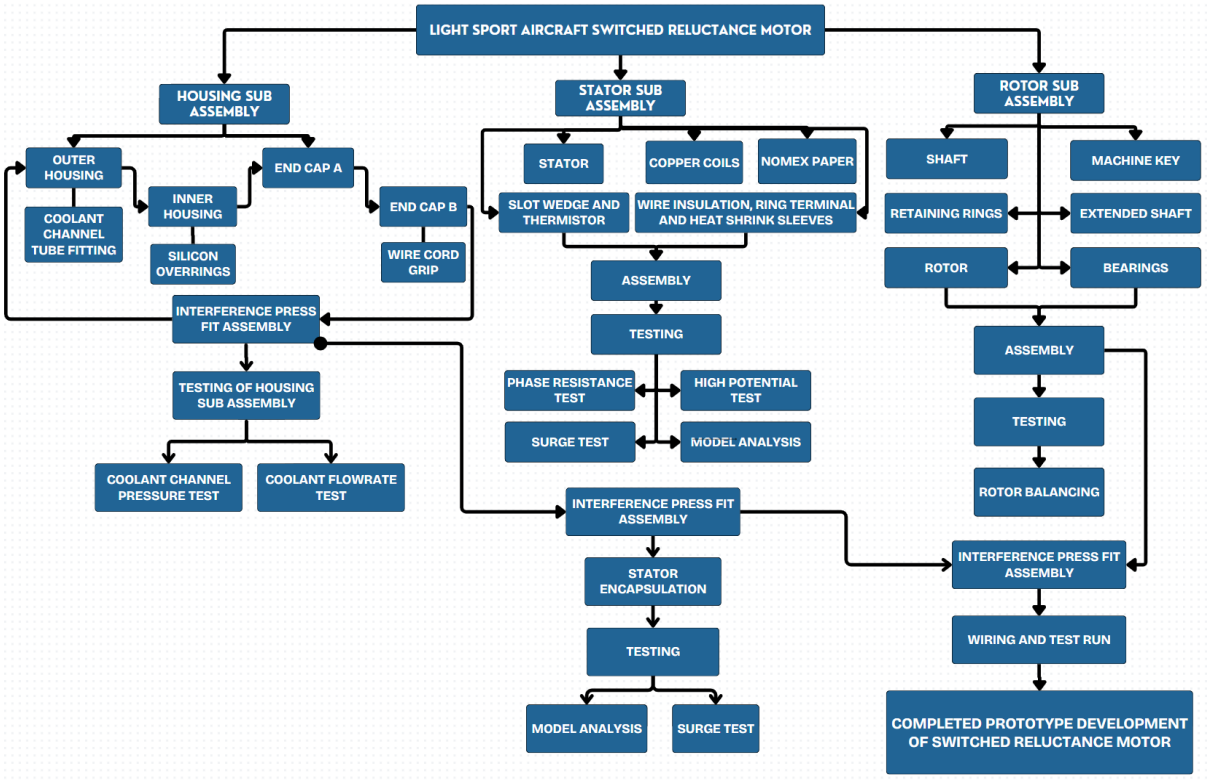

Figure 8 - Manufacturing and Assembly Process

3.1.1 Housing Design

The main physical boundary of the motor is the housing of the LSA SRM. The physical volume of the motor is determined by two key dimensions of the motor housing, the axial length, and the diameter, as shown in *Figure 9*. The mass of the motor housing is often a design limitation. The size of the motor housing and mounting components are determined by several dimensions.

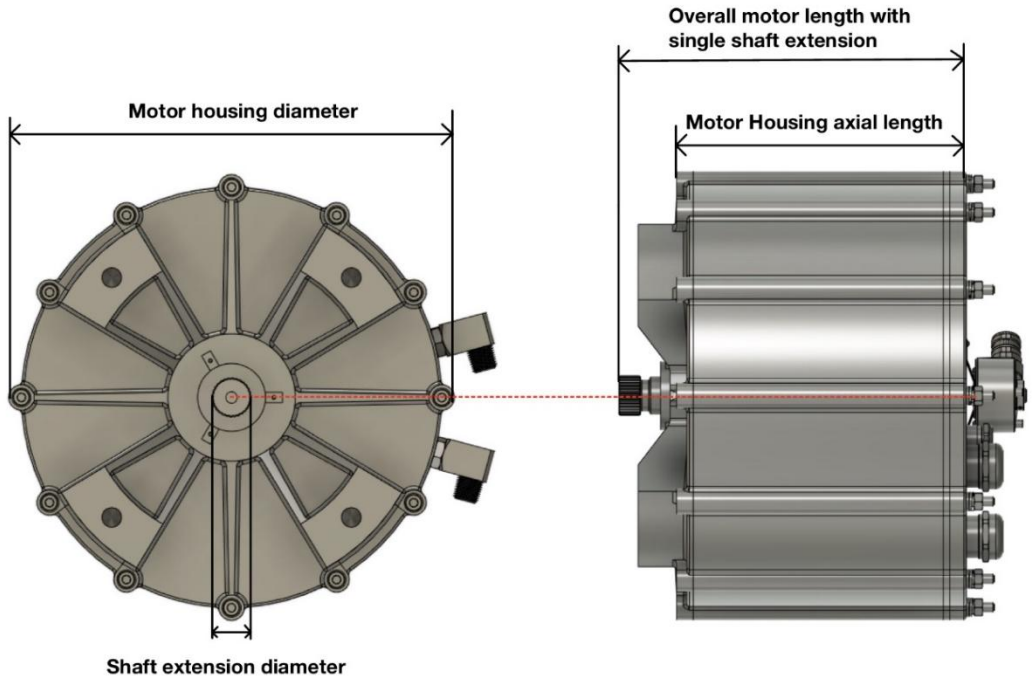

Figure 9 - Key Dimensions of LSA SRM

The stator-winding subassembly volume, enclosure type, and mounting method primarily determine the size of the motor housing. The coolant channel for the cooling process has also been designed into the motor housing design. The housing is intended to enclose the stator and rotor entirely, keep the components cool during

operation, and dissipate heat that conducts and radiates through the housing. The cooling method was chosen based on the power, current density, losses, and allowed temperature rise. *Figure 10* shows the number of layers in the LSA SRM. The shaft-rotor subassembly is in the inner layer. The air gap layer is located between the rotor and the stator. The following layer is the stator-coil winding subassembly. The coolant circulates between the inner and outer housing layers. The inner housing layer separates the stator and the coolant.

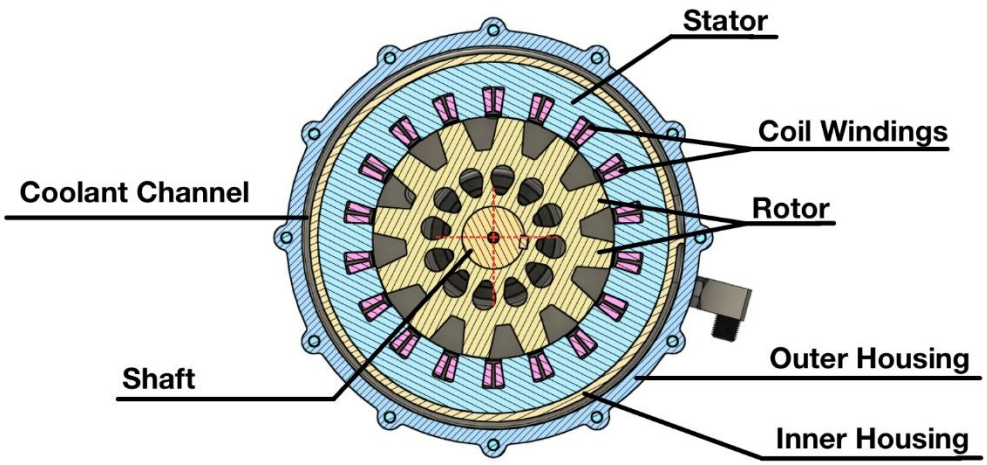

Figure 10 - Layers of LSA SRM with Coolant Channel

The two halves of the housing, as shown in *Figure 11*, are designed to be press-fit together with the O-rings on the outer surface of the inner housing to ensure a tight seal and minimal inter-channel leakage.

Figure 11 - Outer Housing (Left), Inner Housing (Right)

Figure 12 shows the end covers. The Endcap B protects the shaft's rear end and includes an encoder and chord grips for temperature sensors and power cables. The Endcap A supports the shaft's drive end and is mounted on the applicable dyno during testing. A grounding ring is also installed on the Endcap A to reduce bearing currents, which can cause pitting and fluting of the bearing balls.

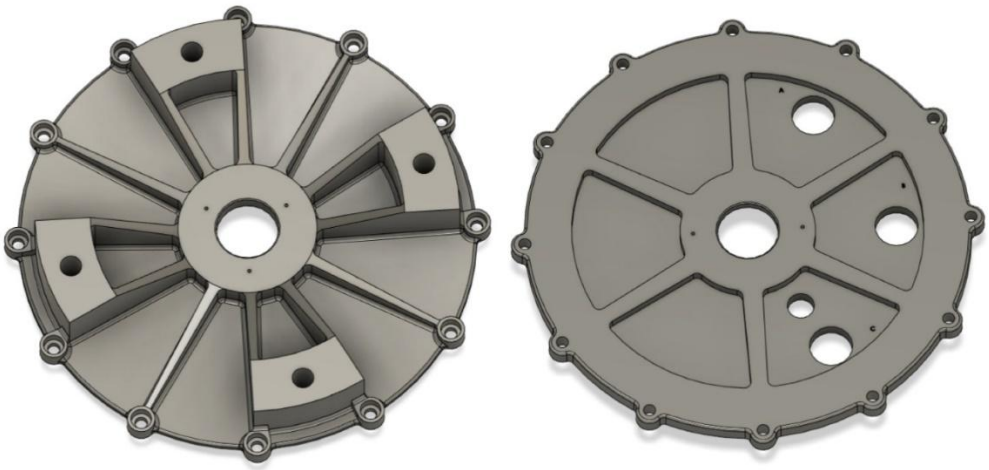

Figure 12 - Endcap A (left), Endcap B(right)

3.1.2 Stator and Rotor Design

The magnetic characteristics of the core material significantly impact SRM performance. The motor's rotor and stator cores should be made of a carefully chosen magnetic core material to increase torque density [7]. Compared to electrical steel, the iron-cobalt-vanadium soft magnetic alloy HIPERCO® 50A has the highest magnetic saturation (24 kilogauss) of any soft magnetic alloy sold commercially while still having a low core loss. The mechanical properties and material composition are shown in *Table 3*. Because of its superior performance and excellent magnetic saturation, the HIPERCO® 50A is chosen as the primary material for this project's rotor and stator design [15].

Table 3 - Properties of HIPERCO® 50A[15]

Material Composition	Iron	49.49%
	Cobalt	48.5%
	Vanadium	2.00%
	Niobium	0.01%
	Carbon	0.001%
Mechanical Properties	0.2% Yield Strength	202MPa
	Ultimate Tensile Strength	498Mpa
	Elongation in 2in	6.7%
	CTE	9.59X10^-6

The stator and rotor design process were guided by the design parameters and configurations shown in *Table 4* [7]. These parameters provide critical information, such as stack length dimensions, airgap length, and dimensions of the stator rotor poles.

Table 4 - Stator and Rotor Configuration[7]

PARAMETER	VALUE
AIRGAP LENGTH	0.4mm
STACK LENGTH	100mm
SHAFT DIAMETER	50mm
NUMBER OF STATOR POLES	18
STATOR POLE ARC ANGLE	13.153°
STATOR POLE HEIGHT	23.6mm
NUMBER OF ROTOR POLES	12
ROTOR POLE HEIGHT	26mm
ROTOR POLE ARC ANGLE	12.74°

The stator and rotor have an 18/12 pole configuration, with 18 on the stator and 12 on the rotor as shown in *Figure 13* . The inclusion of cut-outs in the rotor design is notable, as they significantly reduce the rotor's mass while maintaining its mechanical strength. These cut-outs were placed strategically along the rotor's magnetic flux paths to minimize their effect on the motor's electromagnetic performance. The

design maintains torque output by carefully selecting the placement and shape of these cut-outs, avoiding any significant performance loss. Overall, the rotor cut-outs reduced the motor's mass by 18.4%, or about 3 kg, increasing efficiency and responsiveness while maintaining structural integrity and operational capabilities [7].

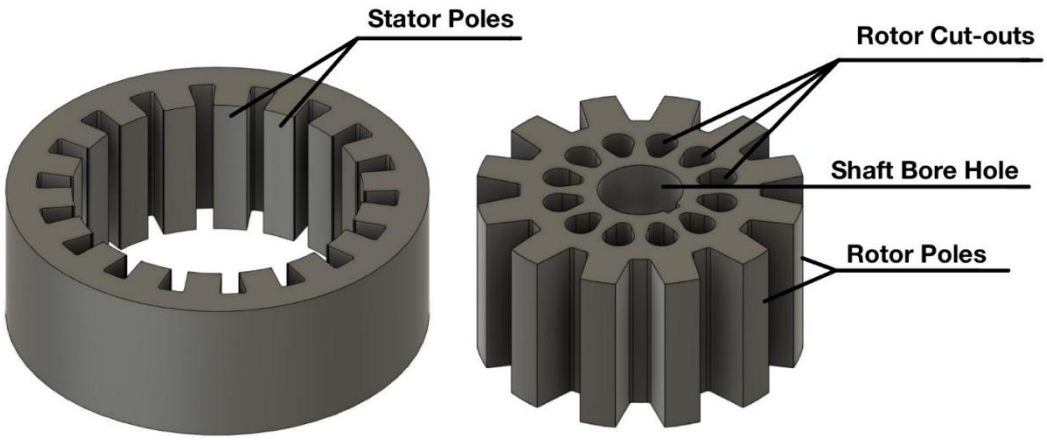

Figure 13 - Stator and Rotor Design

3.1.3 Shaft Design and Loading Conditions

The drive end of the motor shaft has a spline to efficiently transmit torque to the coupling, as shown in *Figure 14*. This design choice distributes the load across multiple teeth along the shaft's circumference, improving torque transmission but it adds some complexity to the manufacturing process. To secure the assembly, a retaining ring restricts the rear bearing and prevents the rotor and shaft from moving axially.

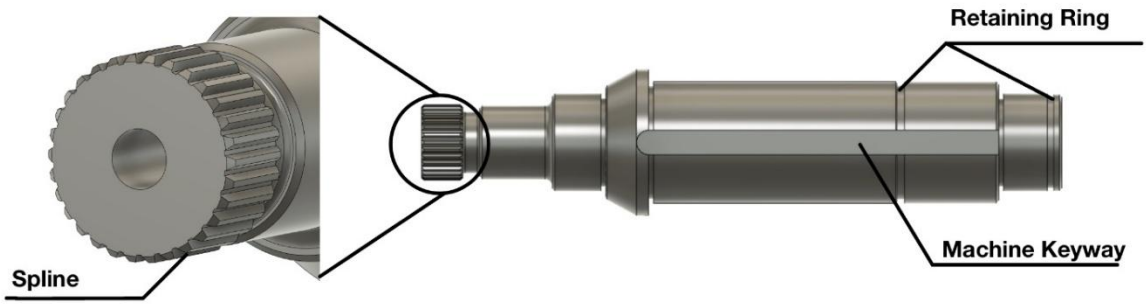

Figure 14 - Shaft Design

The shaft is made of AISI 8620 steel, chosen for its durability and high yield strength of 360 MPa, as shown in *Table 5*. Two features are applied into the shaft to align the rotor and shaft and restrict free movement. However, in a conservative approach, only one of the ways is assumed to carry the entire load during operation. A press fit between the rotor and shaft is primary way when carrying the load. The machine keyway would only engage if the press fit loosened due to high impulse or shocks (vibrations) or elevated operating temperatures, allowing the rotor to expand and loosen its grip on the shaft. An shaft extension is pressed into a bore at the rear end of the main shaft. This extension is an encoder mount that allows for precise position sensing, which is critical to the motor's operation.

Table 5 - Critical Properties of AISI 8620 [17]

Mechanical Properties	Metric Value
Density	7.85 g/cc
Ultimate Tensile Strength	635MPa
Yield Strength	360MPa
Poissons Ratio	0.29
Coefficient of Thermal Expansion	12.2×10^{-6}

3.1.4 Bearing Selection

Bearings and shafts are crucial components of the LSA SRM because they sustain the (rotary motion) rotating rotor and align it both radially and axially with the stator. Due to the small air gap of the SRM (0.4mm), when compared to other motor types, a rigid motor construction is required to provide a consistent air gap. An unequal air gap can result in higher torque ripple, imbalanced radial pull, and undesirable vibration and noise. *Figure 15* shows two KOYO 3NC6208ZZC3 shielded deep groove ball bearings that support the rotor assembly. The dimensions of each bearing are 40 x 80 x 18 mm. These bearings are carefully embedded into the motor end covers. The shaft has a floating bearing arrangement, allowing axial play. This design choice accommodates tolerance stack-up and ensures proper alignment throughout the assembly. A wave spring washer is included to control axial play and ensure assembly stability. The shaft's spline design allows it to connect directly to the test cell, restricting radial shaft

loading. The operating speed of the LSA SRM us relatively low as it is a direct-drive motor. Lack of a gearbox also reduces the thrust loads. This simplifies the bearing requirements at the prototype stage. Despite this simple setup, some eccentricity is expected, which may contribute to radial loading on the bearings, which is estimated to be around 1000 N.

Figure 15 - KOYO 3NC6208ZZC3 Shielded Deep Groove Ball Bearings

3.2 Manufacturing Tolerances

The motor assembly consists of many individual parts that must fit together with extreme precision to ensure peak motor performance. Achieving the proper clearance balance is critical – too much play can result in excessive vibration, premature wear, or even motor failure. On the other hand, too little play can make assembly difficult and cause excessive residual stresses in the components. These stresses may cause unexpected yielding when the motor is subjected to different operational loads. A complete tolerance stack-up analysis is critical to the motor's overall performance. This examination guarantees that all elements are correctly aligned without leaving

excessive gaps or generating interference. It is essential for preventing leaks in the coolant system because even a small misalignments can cause sealing failures. In addition, accurate alignment of the rotor and stator is required to reduce any eccentricity in the motor. Proper alignment not only lowers the possibility of vibration but also allows the motor to attain its full performance potential, assuring smooth and efficient operation for the duration of its life.

3.2.1 Housing Fit

The inner housing consisting of coolant channels along its outer surface and the outer housing were fitted with a medium drive interference fit. This fit has two purposes: (1) it seals the coolant channels between the two layers of housing, avoiding leaks, and (2) provides effective torque transfer from the housing to the motor mounting fixture via the bolts as shown in *Figure 16*.

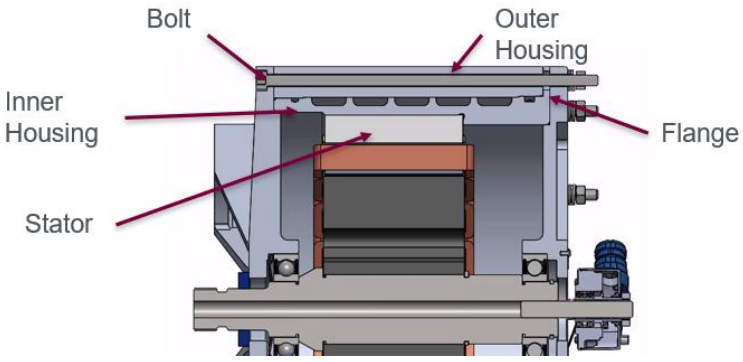

Figure 16 - Torque Transfer to End Cap a Through Bolts

This design choice was validated using FEA under various situations. The FEA ensured that adequate contact pressure was maintained even at maximum operating

temperatures and minimal material contact conditions – when the fit was the loosest. At the other extreme, when the temperature is at its lowest and the material is in its peak contact condition, the analysis revealed that the increased pressure from the interference fit did not cause material yielding. This meticulous examination guarantees that the housing retains its integrity and performance across the entire operating range, balancing the need for a secure fit with the prevention of potential material stress or deformation. *Figure 17* displays the results.

Figure 17 (a) shows the modelled components with a 260 Nm torque load applied to the inner housing bore where the stator sits. Based on the coolant channel's surface area and torque needs, a contact pressure of 290 KPa is required, assuming a coefficient of friction of 0.2 for smooth aluminum. *Figure 17 (b)* shows the peak contact pressure of 49 MPa and an average contact pressure of 5.9 MPa calculated across the surface. This contact pressure is more than adequate to ensure consistent torque transfer. *Figure 17 (c)* shows that there are no gaps between channels, even with the loosest fit, ensuring that coolant is securely contained within the channels and does not leak out of the housing. *Figures 17 (d) and (e)* show the peak stress levels in the inner and outer housing components, reaching 52 MPa and 83 MPa, respectively. Given the yield strength of 6061-T6 aluminum (276 MPa), the design comfortably avoids plastic deformation. To be conservative, contact pressure at the housing flange foot was not considered in this analysis, providing a solid assurance of the assembly's durability and leak-tight integrity.

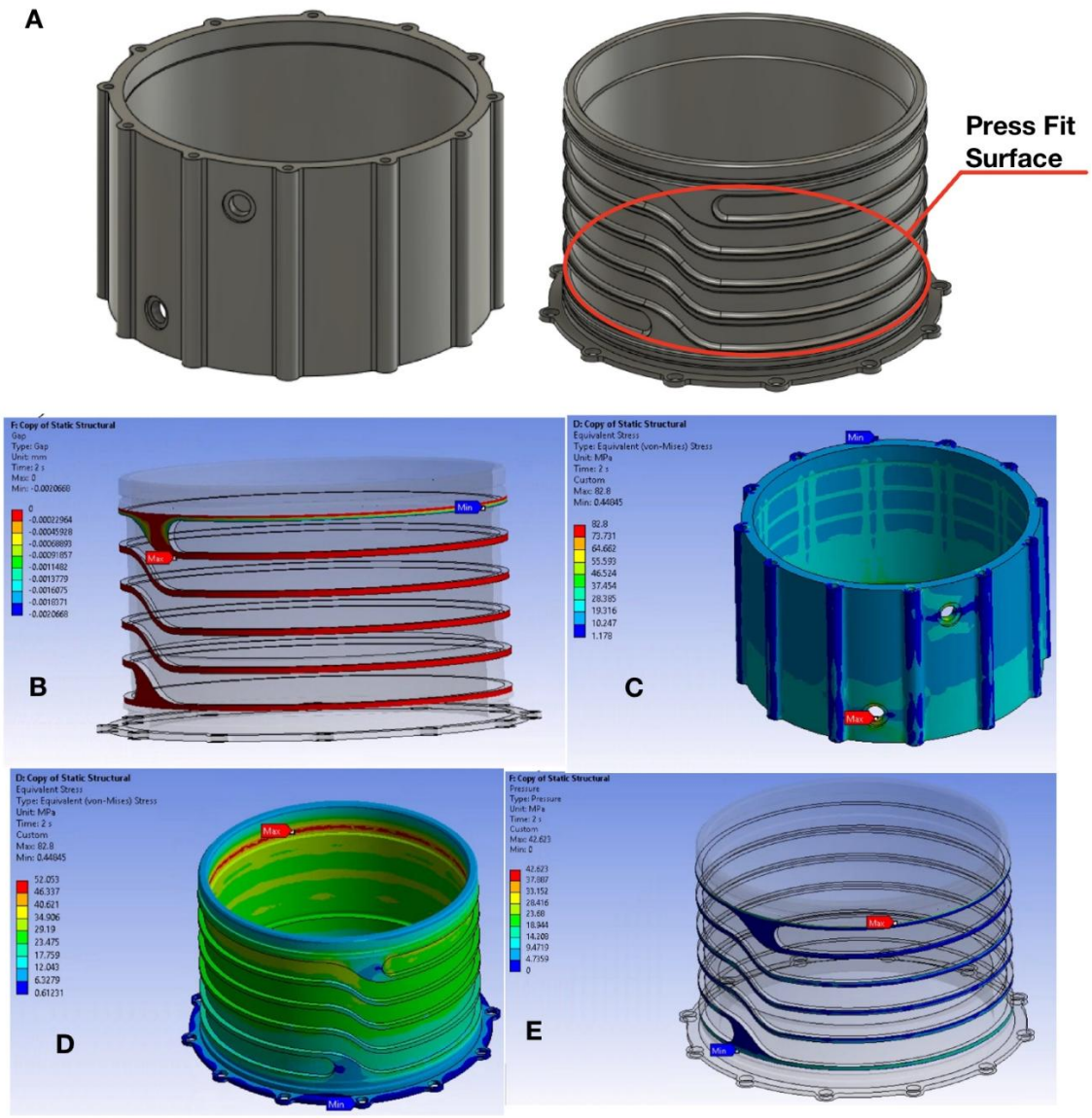

Figure 17 - Housing Press Fit FEA

A press fit analysis was performed on the medium drive interference fit between the stator and the inner housing to ensure adequate contact pressure for reliable torque transfer without damaging the components. The results of this analysis are shown in *Figure 18*.

Figure 18 (a) represents the modelled components with a 260 Nm torque load applied to the stator teeth. For effective torque transfer from the stator to the housing, only 105 KPa of contact pressure is required. *Figure 18 (b)* represents the resulting contact pressure distribution, with a peak contact pressure of 75 MPa and an average of 3.1 MPa at maximum temperature and least material condition (LMC). *Figure 18 (c)* indicates that no gaps form between the stator and housing even under these conditions, ensuring consistent contact and avoiding torque loss. *Figures 18 (d) and (e)* display the peak stress levels in the inner housing and stator, which reach 73 MPa and 59 MPa, respectively. Both stress values are significantly lower than the material's yield strengths (greater than 200 MPa). This finding confirms that the press fit design ensures a secure and dependable torque transfer connection while maintaining the structural integrity of the stator and inner housing.

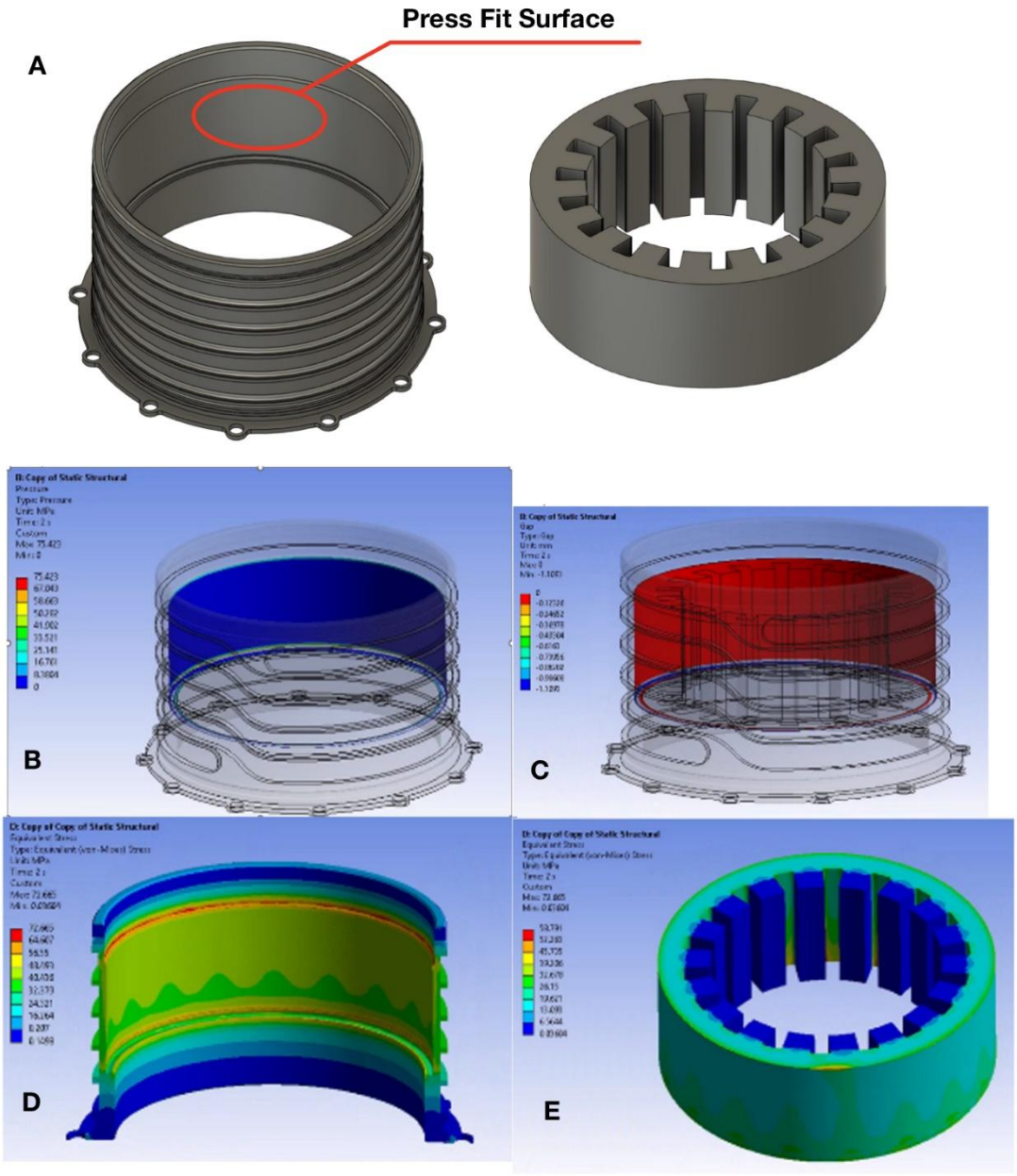

Figure 18 - Stator Press Fit FEA

3.2.2 Endcaps Fit

In the LSA SRM design, the two-piece housing completely encloses the water jacket, so the endcaps are not required to form a watertight seal. However, the endcaps continue to play important roles in the motor's overall functionality. These responsibilities include preventing dust and other contaminants from entering the motor, ensuring proper rotor shaft alignment, providing a mounting surface for the dynamometer plate, and acting as a base for chord grips, encoders, bolts, and bearings.

The housing and endcaps use a clearance fit, H7/h6 defined in the ISO Standards Handbook on limits, fits, and surface properties, provides a locational clearance fit that ensures a snug fit for stationary parts while allowing easy assembly and disassembly [9]. H7/h6 fit, shown in *Figure 19*, allows for easy installation and removal of the rotor assembly as needed. However, this convenience introduces a small risk of rotor misalignment, a reasonable trade-off for ease of assembly and maintenance. This balance of functionality and assembly flexibility keeps the motor efficient and practical.

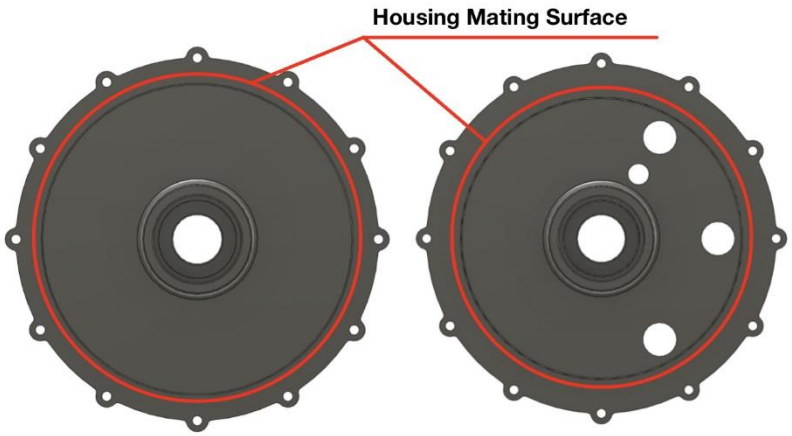

Figure 19 - Mating Surface-Endcap A (left) and Endcap B (right)

3.2.3 Bearing Fit

Among the various machine fits selected for this design, specific components necessitated additional consideration during the design process. One of the primary areas of emphasis was the bearings. A transition fit was chosen to ensure stability and prevent relative movement between the shaft and bearing inner diameters while operating. This fit achieves the proper balance to keep the bearings securely on the shaft.

The manufacturer usually recommends a press fit for the bearing's outer diameter. This is especially important given the material differences: the aluminum motor end cap is more susceptible to thermal expansion at elevated temperatures than the steel bearings it houses. The end cap's expansion may result in excessive play around the bearing's outer diameter without a tight press fit. Despite the high thermal loads, the bearings maintain a secure fit with a press fit. The LSA SRM design also includes a

wave spring washer to apply axial preload to the bearings, allowing for some tolerance in their axial positioning. However, a press fit would interfere with the wave spring washer's function by holding the bearings too tightly. Because the prototype must be assembled and disassembled regularly during its limited lifespan, an F8/h5 clearance fit, as specified in the ISO Standards Handbook on limits, fits, and surface properties is a running fit designed for precise machines. It ensures accurate location at moderate speeds and journal pressures[9] was eventually chosen between the end cap and the bearing's inner diameter. This fit allows easier bearing installation and removal, balancing functionality with practicality. Although this clearance fit may shorten the bearing's life, it is adequate to meet the prototype's intended usage requirements.

3.2.4 Rotor Shaft Fit

Locational interference fits were chosen between the shaft and the rotor to ensure correct alignment and safe torque transfer. This fit provides stability and stops undesired movement by axially and tangentially constraining the rotor under typical operating conditions. As illustrated in *Figure 20*, retaining rings and shaft keyways were included in the design to provide additional redundancy. If the primary interference fit is compromised, these extra features act as backups to keep the rotor in place and operating.

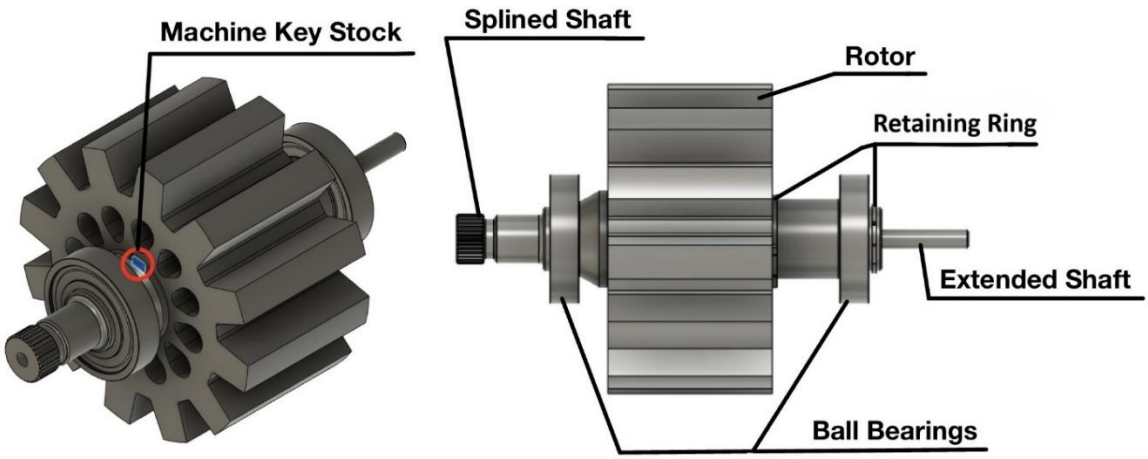

Figure 20 - Rotor Sub-assembly

Achieving the proper balance of contact pressure was crucial, so special attention was given to examining the fit between the rotor and the shaft. To transfer torque effectively, the pressure had to be high enough to generate enough friction without causing the rotor material to yield. The rotor core comprises annealed HIPERCO® 50A, and the shaft comprises AISI 8620 steel. The yield strength of HIPERCO® 50A is 220 MPa and the yield strength of AISI 8620 steel is 360 MPa. Thus, the rotor yield strength is lower than the shaft. It is also crucial to control stress levels carefully because the rotor is more susceptible to increased iron loss due to stress in the rotor back iron.

When a H7/s6 medium drive interference fit, as specified in the ISO Standards Handbook on limits, fits, and surface properties, is a medium drive fit suitable for ordinary steel parts or shrink fits on light sections, representing the tightest fit recommended for use with cast iron, is applied to the joint between shaft and rotor.

Figure 21 shows the rotor stress assessment carried out using FEA. When the interference is at its maximum permissible limit, stress at the inner diameter is more significant than the yield strength of HIPERCO® 50A. This suggested a possibility of material failure in the rotor in specific circumstances, requiring a reassessment of the fit.

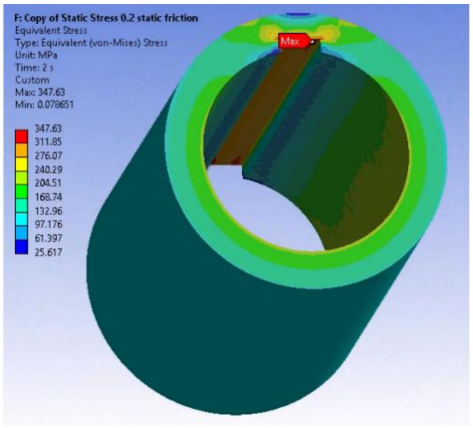

Figure 21 - Cropped rotor stress analysis at the lowest temperature and maximum material condition

This problem was resolved by reducing the interference fit to an H7/p6 (ISO Standards Handbook – Limits, fits, and surface properties – Locational interference fit for parts requiring rigidity and alignment with prime location accuracy, but without special bore pressure requirements [9]), which decreased the rotor's stress levels enough to stop it from yielding. However, under minimum material conditions and maximum operating temperatures – conditions where thermal expansion reduces the interference fit – this interference reduction might not always result in sufficient contact pressure to transfer the necessary torque. The rotor key engages in these

situations to help transmit torque. The key was sized and designed to carry the entire load torque capability to ensure dependable operation even when the interference fit alone is insufficient.

3.2.5 Radial Tolerance

In the worst-case scenario, radial stack-up may cause the rotor to not fit into the stator bore once the assembly is completed or it may create enough play for the rotor to shift while operating and potentially collide with the stator. Mild to moderate rotor eccentricity, which can be static or dynamic, is most often caused by radial stack-up. Because of this eccentricity, the air gap between the rotor and stator varies around the rotor's circumference, closer to the stator at some points and further away at others.

Changes in the air gap can significantly impact performance, resulting in lower torque output, more torque ripple, and higher noise, vibration, and harshness (NVH). A general tolerance guideline is used to mitigate these risks, allowing for a 25% variation in nominal air gap widths. This SRM has an air gap of 0.4 mm and an acceptable tolerance of ±0.1 mm [9]. To achieve this level of precision, all stack components, particularly the rotor and stator, which consist of hundreds of individual laminations, must be of manufactured with high tolerance. These laminations are bonded axially to form a cohesive stack, but variations in stack length can cause minor inconsistencies. Ensuring that these tolerances are maintained throughout the assembly is critical for maintaining optimal performance and avoiding eccentricity. *Figure 22* shows a partial radial stack-up. Numbers *5* and *6* present the radial

tolerance of the housing and stator, while *15* and *16* depict the radial tolerance of the rotor and shaft. Number *3* highlights the radial tolerance between the stator and rotor, and *7* demonstrates the tolerance between the end cap and housing. Additionally, *9* and *10* show the fit between the bearing and end cap, and *12* illustrates the fit between the bearing and shaft.

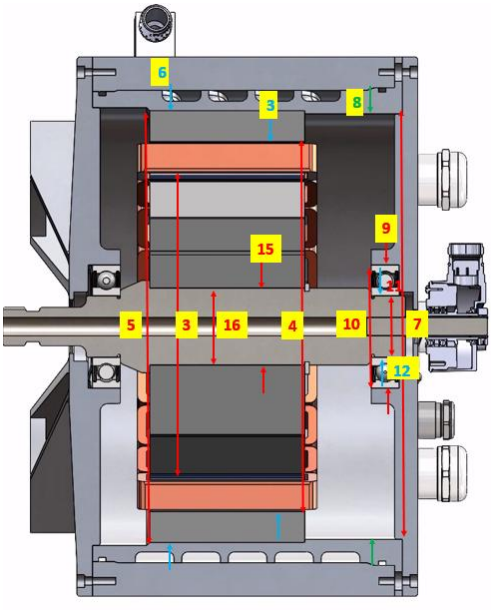

Figure 22 - Radial Stack Up Tolerances

3.2.6 Axial Tolerance

Poor axial tolerances in an SRM can result in torque loss and unwanted vibrations. This usually happens when the rotor becomes axially misaligned relative to the stator, reducing magnetic flux and causing axial magnetic pull forces. The rotor is typically designed to be slightly oversized in the axial direction relative to the stator to avoid

these issues. This oversizing ensures that the rotor remains aligned during operation, regardless of any inherent play in the assembly.

In this case, the stack-up analysis determined that an additional 2 mm rotor stack – equivalent to 14 laminations—was required to account for potential axial variance. *Figure 23* illustrates a partial axial stack-up analysis. Numbers *1, 2, 9, 8, and 15* present the axial tolerance of the bearings and end caps, while *18* highlights the stator's axial length, and *7* depicts the rotor's axial length. Number *3* shows the axial length of the shaft between the bearings, *11 and 12* illustrate the axial fit between the inner and outer housings. Once the relative axial variance of the rotor assembly was determined, the wave spring washer installed in the endcap bearing bore was sized to ensure a constant bearing axial preload. This preload ranges from a minimum of 40 N to a maximum of 160 N, or one to four times the diameter of the bearing bore. Given the prototype's expected short lifespan, the preload was intentionally kept low to make assembly easier.

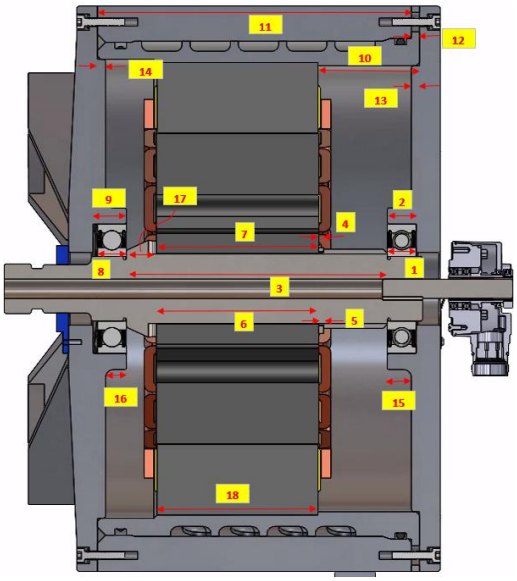

Figure 23 - Axial Stack Up Tolerance

3.3 Summary

The detailed mechanical design focuses on the structural and functional optimization of the LSA SRM, using advanced materials and precision engineering to achieve strict tolerances. The housing was designed to contain coolant channels for efficient thermal management while remaining compact. Stator and rotor design use high-performance materials such as HIPERCO® 50A to improve magnetic efficiency and torque density. Bearings, shaft design, and fit are selected to reduce vibrations and ensure consistent performance. FEA analyses validate structural integrity under various operational stresses, confirming the reliability of interference fits and assembly decisions.

CHAPTER 4- MANUFACTURING OF THE LSA SRM COMPONENTS

After finalizing the structural design and determining the manufacturing tolerances, the focus moves to manufacturing the motor components. This chapter goes into the manufacturing procedures used to make these components accurately and with high quality. Each component is crucial to assuring the motor's overall performance and reliability, and its manufacture requires precise attention to detail, adherence to required tolerances, and the use of appropriate materials and methods.

4.1 Housing Manufacturing

4.1.1 Material Selection of Housing

Aluminum and its alloys are well-known in various industries due to their unique characteristics. These include an appealing appearance, lightweight, fluidity, and exceptional casting ability. Aluminum is also highly fabricable, with balanced physical and mechanical qualities and resistance to hot tearing and corrosion. These outstanding qualities make it the ideal material for applications in aerospace industries. A356-T6 cast aluminum alloy was chosen for the motor housing because it meets the specific requirements of this application. These requirements include meeting the properties of wrought aluminum 6061, which A356-T6 does, while

costing less than wrought aluminum. Wrought aluminum has excellent properties but it is expensive for components such as motor housing. A356-T6 offers a practical alternative with comparable performance at a lower cost, making it a good choice for this application. A356 belongs to the 3xx.x series of aluminum alloys, specifically the Al-Si-Mg casting alloys. This alloy is further improved with a T6 temper, a heat treatment process that hardens and strengthens the material, making it suitable for high-performance uses. A356-T6 is widely used in the automotive and aerospace industries due to its versatility, which combines strength, lightweight properties, and corrosion resistance. *Figure 24* depicts the mechanical and chemical properties of A356-T6 [19].

Chemical Properties																			
Designation		Products	Sa	Fe	Cu	Mn	Mg	Si	Ni	Zn	Ti	Ag	Be	Pb	Sn	Zr	Others		Al
AA.No	Date Registered																Each	Total	
A356 0	-	S&p	6.5-7.5	0.2	0.2	0.10	0.2-0.4			0.1	0.2						0.05	0.15	

Mechanical Properties							
Alloy	Temper	Tensile Strength				% Elongation in 2 in or 4 times diameter	Typical Brinell Hardness 500 –kgf Load 10 – mm ball
		Ultimate ksi	Ultimate MPa	Yield (0.2% Offset) ksi	Yield (0.2% Offset) MPa		
A356.0	T6	34.0	235	24.0	165	3.5	70-105

Figure 24 - Properties of A356-T6 [19]

4.1.2 Casting of Housing Components

The casting pattern for the housing subassembly was designed in a near-net shape, assuming a casting shrinkage of 1.5% for the A356 material. This approach ensured

that the casting closely matched the final dimensions after cooling. To optimize manufacturing costs, only the mating surfaces of the cast parts were machined down, leaving other areas as cast. Figure 25 illustrates the additional material added between the housing prototype design and the casting model to account for machining and shrinkage, particularly for the four components of the housing subassembly.

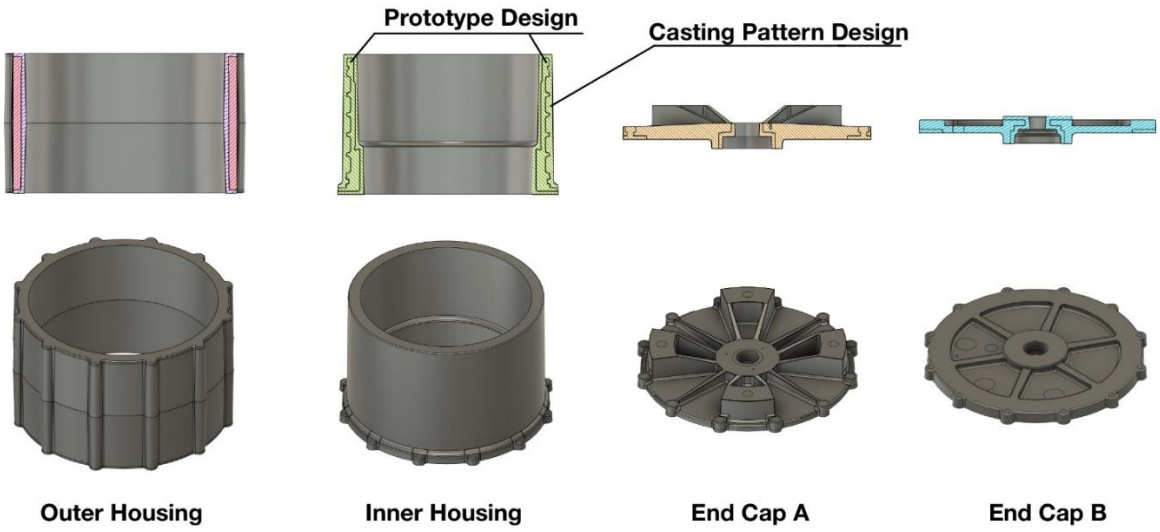

Figure 25 - Section view of casting pattern design

The casting pattern was designed, and then CNC machined with a polyurethane tooling board, as shown in *Figure 26*. This material was chosen for its cost-effectiveness and ease of manufacturing. The polyurethane tooling board is quite multipurpose, allowing precise cutting and shaping to meet the desired design specifications. Its properties allow CNC machining to achieve high precision, ensuring the casting pattern meets the required dimensional tolerances and surface finish.

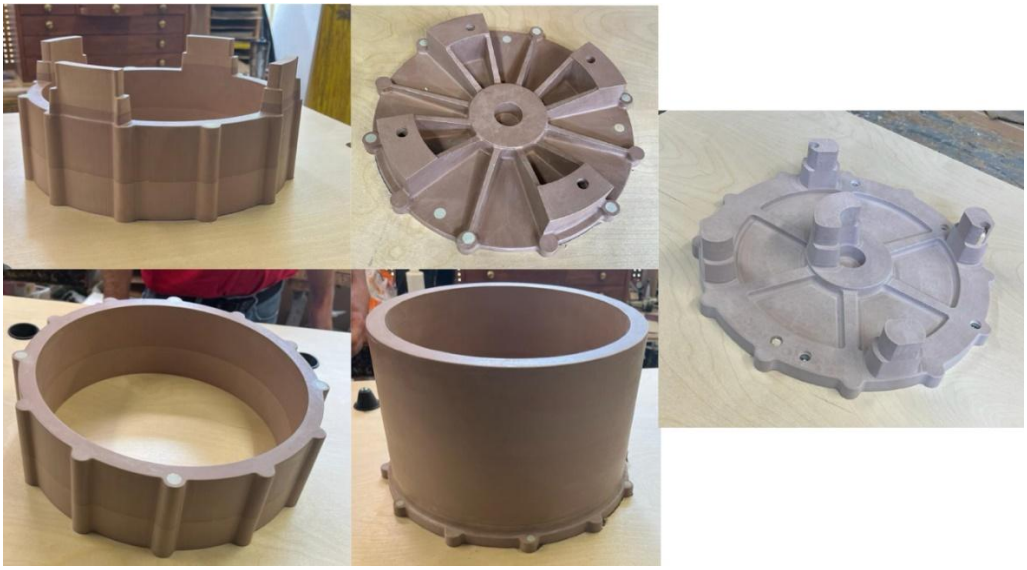

Figure 26 - Polyurethane tooling board casting pattern

Sand casting was chosen as the method of manufacturing the housings. A casting pattern leaves a negative imprint in the sand during this process. The pattern is mounted on a plywood base and inserted top-down into the sand to create the desired outcome. After the impression is completed, the pattern is carefully removed. Air escape passages, which are critical for ensuring proper ventilation during the casting process and preventing defects such as porosity, are then created. Molten metal is then poured into the sand mold's cavity, filling the imprint, and allowed to cool for solidifying. Following cooling, the casting is carefully post-processed, including removing excess material from the air escape passages. Finally, a T6 tempering process in which the cast is heated to 540°C for 10 hours is used on the housings to improve their mechanical properties, ensuring strength and durability for the motor application. *Figure 27* shows the housings after casting.

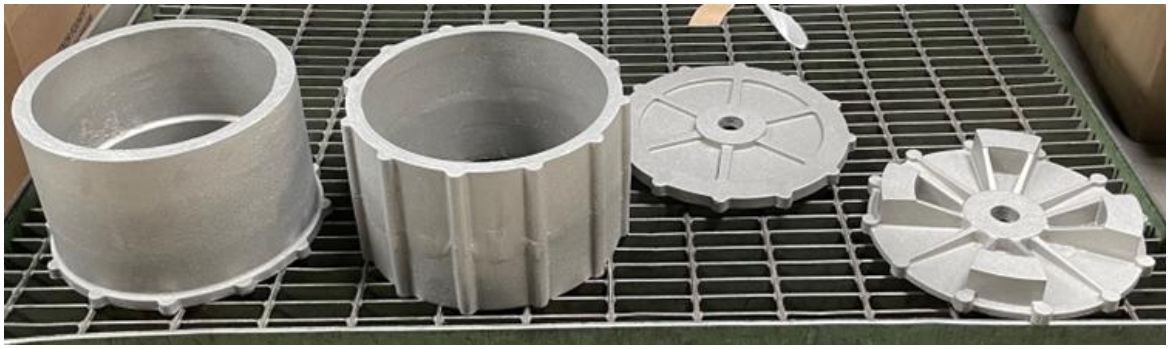

Figure 27- Sand Casted Housings

4.1.3 Machining of Housings

Fixtures used to mount the housings onto the CNC machine were designed and manufactured from aluminum 6061, selected for its strength and machinability. Before machining, the cast housings were thoroughly inspected to ensure dimensional accuracy and structural integrity. The housings then underwent high precision machining processes, including CNC milling and turning, which were performed with utmost precision to achieve the required tolerance and ensure the accuracy of the final product. Chromium nitride-coated carbide tools were used during the machining process to provide a superior surface finish and prevent the formation of built-up edges on the tools. *Figure 28* illustrates the housings during and after machining, highlighting the transformation from cast to finished components.

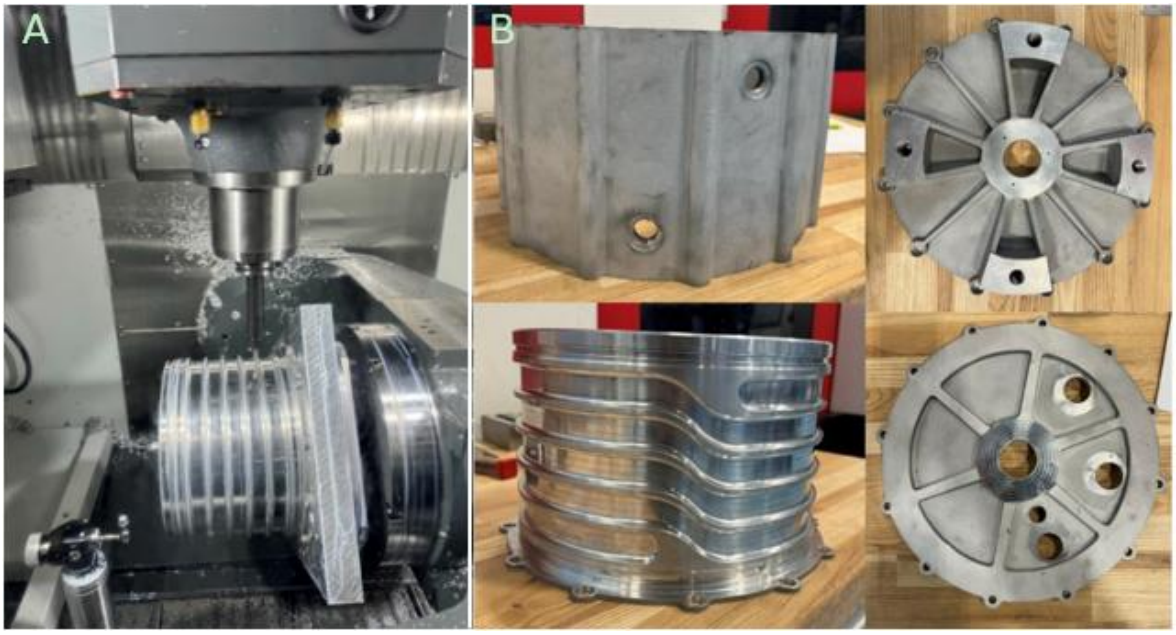

Figure 28 – (a) Housings During Machining and (b)Housings After Machining

4.1.4-Dimensional Inspection of Housings

The critical dimensions of the housing components were thoroughly examined with a Coordinate Measurement Machine (CMM). This process ensured high precision and accuracy in determining whether the manufactured components met the required specifications. The CMM measurements were compared to the nominal dimensions to identify any deviations. *Table 6* compares the nominal dimensions to the measured values, showing the machining process's consistency and accuracy.

Table 6 - Housings Nominal Values vs Measured Values

Part	Nominal value (mm)	Measured value (mm)	Tolerance(mm)	Deviation (mm)	Status
Inner Housing (Inner Diameter where Stator meets)	280.026	280.0015	±0.026	0.0245	Within Tolerance
Inner Housing (Outer Diameter)	305.85	305.838	+0, -0.032	-0.012	Within Tolerance
Outer Housing (Inner Diameter)	305.674	305.6677	±0.026	0.0063	Within Tolerance
End Cap (Bearing Bore)	80	80.0528	+0.0760, -0.0300	0.0528	Within Tolerance
End Cap (Housing Cover Flange)	284	284.19	+0.00, -0.032	0.19	Exceeding Tolerance

4.2 Rotor and Stator Core Prototypes

HIPERCO® 50Alaminations with a thickness of 0.152 mm were laser cut and then stacked and bonded together to achieve the desired stack length of 100 mm. Additionally, the outer surface of the stator was cylindrical ground to achieve a surface finish, ensuring proper fit with the housing. *Figure 29* shows the completed stator and rotor cores.

Figure 29 - Stator and Rotor

4.2.1-Dimensional Inspection of Rotor and Stator

A CMM was used to examine the critical dimensions of the rotor and stator meticulously. The accuracy of the measurements was checked by comparing them to the nominal dimensions. *Table 7* gives a thorough overview of the stator and rotor dimensions. It also displays the findings of the inspection and confirms that the component dimensions meet the design specifications.

Table 7 - Stator And Rotor Inspection Report

Part	Nominal value (mm)	Measured value (mm)	Tolerance(mm)	Deviation (mm)	Status
STATOR (Outer Diameter)	280.174	280.156	±0.0160	-0.018	Within Tolerance
STATOR (Inner Diameter)	192.8	192.8366	±0.05	0.0366	Within Tolerance
STATOR (Stack Length)	100	100.1509	±0.1520	0.1509	Within Tolerance
ROTOR (Stack Length)	102.0873	102.13	±0.05	-0.0427	Within Tolerance
ROTOR (Bore Hole Diameter)	50.0125	50.0373	0.03	0.0248	Within Tolerance
ROTOR (Bore Hole Edge to Edge Stack Length)	105.0032	102.13	±0.05	2.8732	Exceeding Tolerance
ROTOR (Outer Diameter)	192	192.06	±0.10	0.06	Within Tolerance

After inspecting the rotor and stator, it was observed that the rotor bore edge had deformations caused by cutting forces during the drilling process for the shaft bore. This deformation resulted in an extra 1.7804 mm and 1.0928 mm extrusion on both bore sides.

4.3 Manufacturing of the Shaft

The shaft was precision CNC machined from AISI 8620 steel to the required tolerances of 50.051 mm (+0.051/-0.032 mm) at the shaft-rotor interface. These tight tolerances ensured a precise fit for peak performance and alignment. The shaft's spline was carefully machined to withstand the 260 Nm torque expected during testing, ensuring consistent torque transmission without failure. *Figure 30* shows the manufactured shaft.

Figure 30 - Manufactured Shaft

The dimensional inspection results using a CMM showed a 50.095 mm measurement for the surface where the rotor sits. This measurement is within the design tolerance, indicating that the component meets the specifications and ensures proper fit and functionality in the assembly.

4.4 Coil Winding

The geometry and coil configuration were designed to deliver the required performance while meeting the prototyping constraints. Double-insulated copper wire MW35-C with a 17 AWG wire gauge was applied for its electrical properties. Each

coil had 83 turns, resulting in a slot fill factor of 59%, efficiently using the available space [7].

The motor's three-phase design includes six parallel coils for each phase, for a total of 18 coils. The coils were machine wound to ensure consistency and precision during manufacturing. *Figure 31* shows the completed coil winding.

Figure 31 - Wound Coils of the LSA SRM prototype

4.5 Slot Wedges

A slot wedge design was applied to secure the coils within the stator slots, as shown in *Figure 32.* The material for the slot wedge was chosen for its mechanical robustness and thermal resistance, ensuring it could effectively hold the coils in place under operational conditions. The dimensions of the grooves for the slot wedges were set to 0.8 mm in width and 0.5 mm in depth, positioned 1 mm away from the edge of the stator teeth.

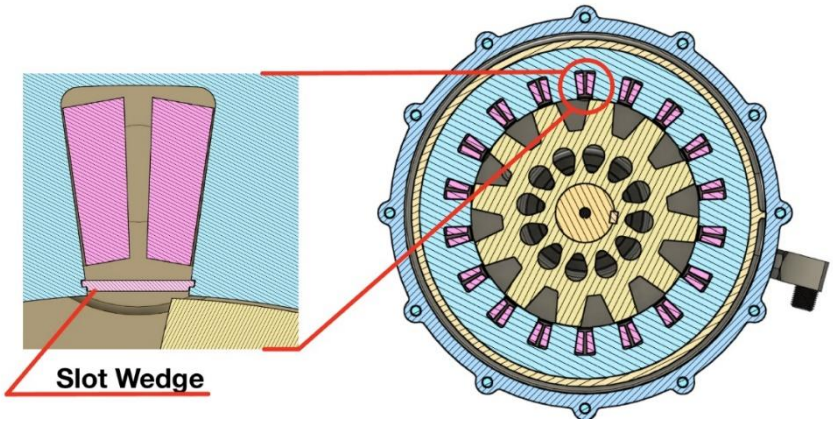

Figure 32 - Slot Wedge Functionality

Several materials were evaluated based on thermal properties and manufacturability as detailed in Table 8.

Table 8 - Material Selection for Slot Wedge

Material	PLA	PA6 GF30	PA6 GF40	PA6 CF30	DELRIN	ACETAL	Durafoam GF
Glass Transtion Temperature	60°C	70°C	72°C	75°C			110°C
Melting Point	165°C	220°C	220°C	220°C	175°C	160°C	175C
Manufacturing Method	3D Printer	3D Printer	3D Printer	3D Printer	Machining	Machining	Additive manufacturing SLS

After a thorough analysis, PA6-GF30 reinforced nylon-based polymer, a nylon-based glass fiber 30% reinforced material, was selected as the most suitable due to its excellent thermal resistance, mechanical strength, and cost-effectiveness. *Figure 33* illustrates the 3D-printed slot wedge with infill density of 50%.

Figure 33 - 3D Printed Slot Wedges

4.6 Summary

The LSA SRM components were manufactured with precision and attention to detail to meet design and operational standards. The housing, rotor, stator, and shaft were made from high-strength materials, thermal- -conductivity, and magnetic properties. Advanced manufacturing techniques, such as high-precision machining and casting, ensured that the components remained within tight tolerances. Dimensional inspections with a Coordinate Measuring Machine (CMM) confirmed the accuracy of critical dimensions and that most components met the specified tolerances. Iterative

adjustments and innovative approaches addressed interference fit and dimensional inconsistencies.

CHAPTER 5- ASSEMBLY OF THE LSA SRM AND FUNCTIONAL VALIDATION OF THE ASSEMBLY COMPONENTS

5.1 Housing Sub Assembly

The two-part motor housing, which includes inner and outer housing, is designed with an interference fit to ensure a secure and leak-free assembly, as shown in *Figure 34*. O-rings are installed on both ends of the inner housing to prevent coolant leakage from the housing assembly. This design ensures the coolant remains within the housing despite operating pressures and thermal loads. The housing dimensions are critical for achieving the desired interference fit. The outer housing has an inner diameter of 305.6677 mm, while the inner housing has an outer diameter of 305.838 mm, resulting in an interference of 0.1703 mm.

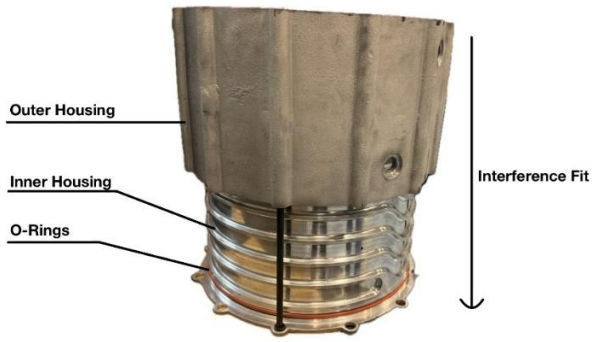

Figure 34 - Housing Assembly Process

The outer housing is heated during assembly, while the inner housing is cooled to allow for thermal expansion and shrinkage. Heating the outer housing expands it, increasing its diameter and allowing the inner housing to fit firmly. Simultaneously, cooling causes the inner housing to shrink slightly, reducing its diameter and making insertion easier. This thermal approach ensures a precise and stress-free assembly while preserving the interference fit when the housings return to the ambient temperature.

The following sections cover the thermal calculations for the necessary heating and cooling, as well as the detailed assembly process. These calculations consider the housing's material properties and the desired interference levels to achieve a secure fit while avoiding excessive stress and deformation.

5.1.1 Thermal Expansion Calculation

The thermal expansion of the components is calculated using the formula [18].

ΔD= Initial Diameter X CTE X ΔT

Where:

T1(°C) - Initial Temperature

T2(°C) - Final Temperature

ΔT(°C) - Change in Temperature (T2-T1)

ΔD(mm) - Change in Diameter

CTE - Coefficient of Thermal Expansion for the material

Table 9 - Housing Thermal Expansion Calculations

Outer Housing (Inner Diameter)	Inner Housing (Outer Diameter)
Material -A356 T6 Aluminum Initial Diameter (mm)= 305.6677mm CTE=21.4 $X10^{-6}$ T1(°C) = 25°C T2(°C) = 110°C ΔT(°C) = 85°C ΔD= 305.6677 X 0.0000214 X 85 **ΔD(mm)= 0.5560mm**	Material -A356 T6 Aluminum Initial Diameter (mm) = 305.838mm CTE=21.4 $X10^{-6}$ T1(°C) = 25°C T2(°C) = -20°C ΔT(°C) = -45°C ΔD= 305.838 X 0.0000214 X -45 **ΔD(mm)= -0.2945mm**
Final Diameter(mm)= 306.2237mm	**Final Diameter(mm)= 305.5434mm**

5.1.2 Assembly Process

As shown in *Figure 35*, the outer and inner housings were heated and cooled, respectively, to their respective target temperatures using the thermal expansion calculations.

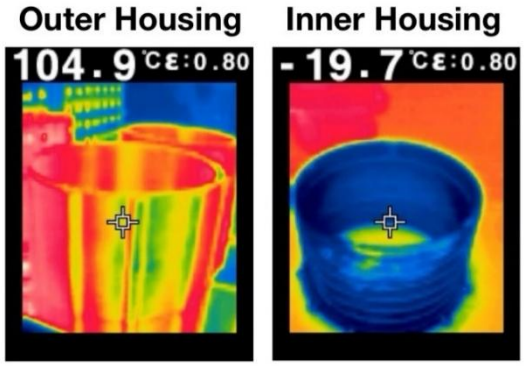

Figure 35 - Thermal Picture of Housing

After the housings were thermally conditioned and aligned for assembly, they were brought together as part of the fitting process. However, a challenge was encountered during the final 8.19 mm of the assembly due to resistance from the O-rings. To overcome this, a hydraulic press was employed, applying up to 8 metric tons of pressure to complete the assembly without damaging the housings or compromising the integrity of the O-rings, as illustrated in *Figure 36.*

Figure 36 - Housing Assembly Process

5.1.3 Air Pressure Test

The assembled housing was pressure tested to ensure its integrity and fully sealed without leaks between the inner and outer housing. *Figure 37* shows the induction of 30 psi air pressure into the housing and maintaining of that pressure for 24 hours. This test was critical to ensure that the housing remained sealed during coolant flow operations and prevented any potential leaks. To facilitate the air pressure test, a custom plug was designed to seal the inlet and outlet valves, ensuring that no air leaked through these openings during the test. This process ensured that the housing was reliable and ready for coolant flow testing.

Figure 37 - Air Pressure Test

5.1.4 Coolant Channel Pressure Test

Following the air pressure test, the coolant flow and pressure inside the housing were tested, which showed that the housing maintained the necessary pressure. The necessary fixtures, including pressure gauges on the inlet and outlet hoses, were made to precisely monitor the pressure levels as shown in *Figure 38*. The coolant temperatures were set at 5°C and 55°C, respectively, and the system was tested at a flow rate of 12 Litres per Minute (LPM).

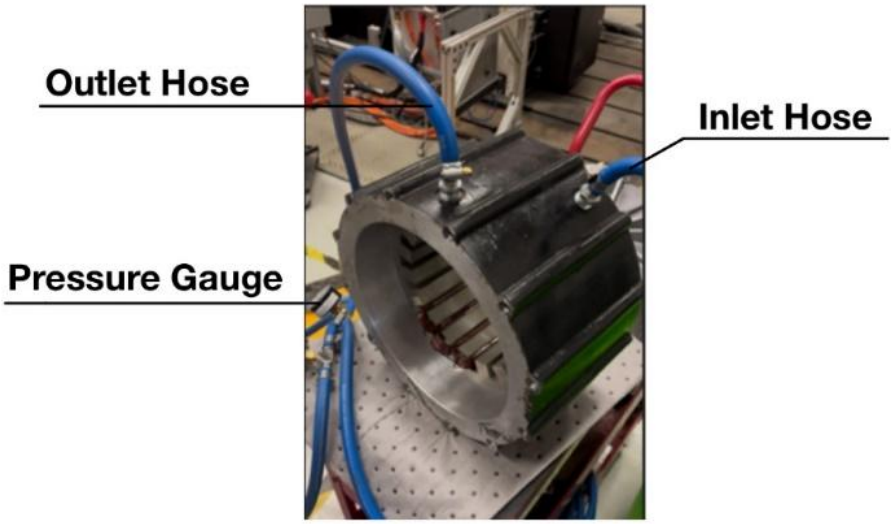

Figure 38 - Coolant Flowrate Test Fixture

This test procedure allowed for measuring changes in the housing temperature and pressure while it was in use. As shown in *Figure 39*, with a coolant flow rate of 12 LPM, the coolant temperature at 55°C results in an inlet pressure of 40 psi and an outlet pressure of 20 psi. When the coolant temperature decreases to 5°C, the inlet pressure

increases to 50 psi, and the outlet pressure rises to 30 psi. This ensures the coolant does not leak from the housings, even under high pressure.

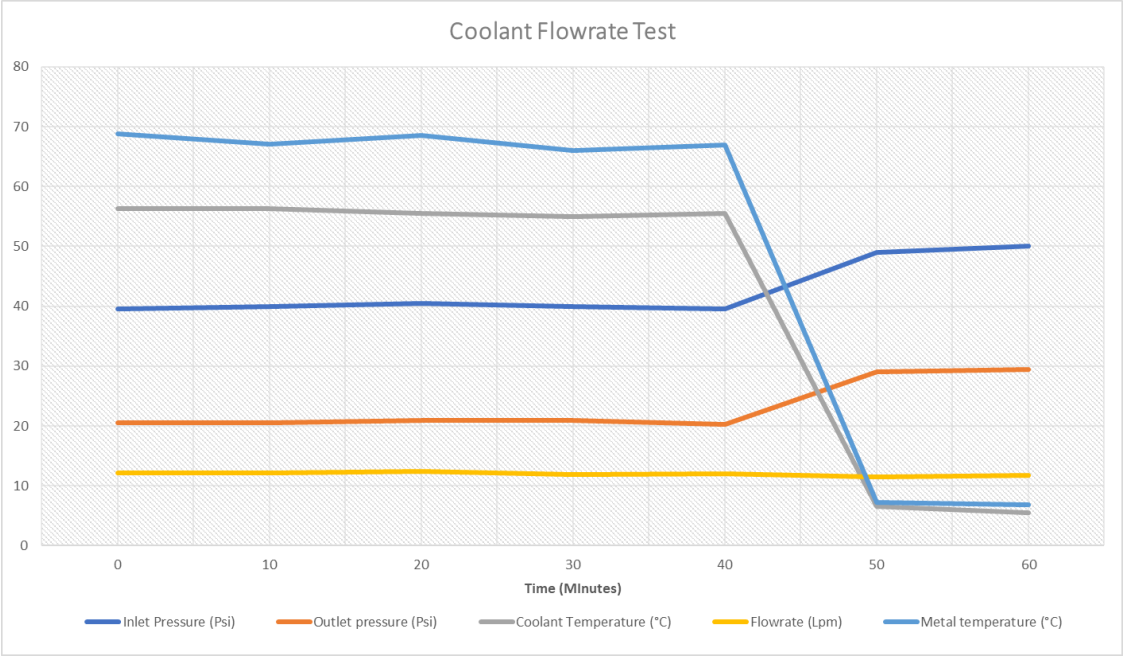

Figure 39 - Coolant Flow Rate Test Results

After assembling and testing the housing subassembly, it was found that the inner diameter of the inner housing had decreased due to interference fit and material movement during the assembly process. Initially, the inner diameter of the inner housing was determined to be 280.0015 mm, as confirmed by the dimensional inspection. However, after assembling the housings, the inner diameter decreased to 279.3117 mm.

This reduction in diameter makes it difficult to assemble the stator into the housing, compromising the precise fit required for proper alignment and functionality. To

address this issue, the inner diameter of the inner housing should be machined following the assembly process. This post-assembly machining step reduces the need for rework, lowers machining costs, and maintains the precise dimensions of the housing, ensuring a seamless stator assembly.

5.2 Rotor Sub Assembly

The rotor subassembly is one of the most critical parts of the motor, requiring precise alignment to meet axial and radial tolerances. This subassembly includes several critical components, such as the shaft, rotor, retaining ring, machine key, and bearings. Each component is critical to the motor's overall performance.

Figure 40 shows the insertion of the rotor and shaft, which is designed as an interference fit. This fit is critical for transferring torque from the rotor to the shaft, especially at high rotational speeds requiring stability and precision. The shaft is immersed in liquid nitrogen to ensure smooth, accurate assembly and to cause shrinkage through thermal contraction. This process temporarily reduces the shaft's diameter, allowing it to fit more quickly and seamlessly into the rotor.

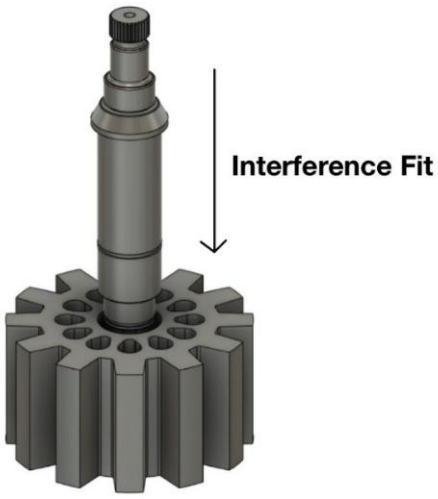

Figure 40 - Design of Rotor Shaft Insertion

When the shaft is inserted and returned to ambient temperature, the interference fit is restored, resulting in a secure and robust connection capable of withstanding the high stresses of motor operation.

5.2.1 Thermal Contraction Calculation

The rotor has a borehole with a diameter of 50.0373 mm, which can accommodate a shaft with a diameter of 50.095 mm. To achieve a secure interference fit, the shaft is thermally contracted by cooling it in liquid nitrogen. Thermal contraction calculations for this process are shown in *Table 10*.

Table 10 - Shaft Thermal Contraction Calculation

Shaft Diameter
Material -AISI 8620 STEEL Initial Diameter (mm)= 50.095mm CTE=12.2 $X10^{-6}$ T1(°C) = 25°C T2(°C) = -100°C ΔT(°C) = -125°C ΔD= 50.095 X 0.0000122 X -125 **ΔD(mm)= -0.0763**
Final Diameter(mm)= 50.0186mm

5.2.2 Challenges in Rotor Shaft Insertion

The shaft was cooled with liquid nitrogen to cause thermal contraction, which allowed it to be inserted into the rotor. However, due to the small clearance (0.018mm) between the rotor and shaft, the assembly process encountered a problem. The shaft became stuck after being inserted about 10 mm into the rotor, as shown in *Figure 41*.

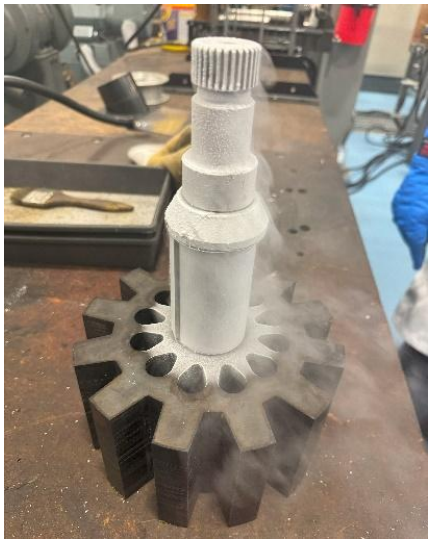

Figure 41 - Failed Rotor Shaft Insertion

A custom fixture made of steel held the rotor securely in place, allowing the shaft to be safely removed without damaging the rotor laminations. As shown in *Figure 42,* a hydraulic press was used to carefully remove the shaft from the rotor while ensuring that the rotor's structural integrity was not compromised.

Figure 42 - Hydraulic Press to Remove Shaft from Rotor

The interference between the rotor and shaft was then recalculated to meet ISO's locational interference fit standards. The shaft diameter was reduced from 50.095mm to 50.064mm using cylindrical grinding. This adjustment refined the dimensions, lowering interference to a level suitable for assembly while maintaining the required performance standards. The recalculated thermal contraction calculations are shown below.

Table 11 - Shaft Thermal Contraction Re-Calculation

The Shaft Diameter
Material -AISI 8620 STEEL Initial Diameter (mm)= 50.064mm CTE=12.2 $X10^{-6}$ T1(°C) = 25°C T2(°C) = -100°C ΔT(°C) = -125°C ΔD= 50.064 X 0.0000122 X -125 **ΔD(mm)= -0.0763**
Final Diameter(mm)= 49.987mm

5.2.3 Rotor Shaft Insertion

After recalculating the thermal contraction and making the necessary adjustments, the shaft was dipped again in liquid nitrogen for the required thermal shrinkage. The rotor was smoothly inserted into the shaft without any issues due to clearance 0.050 mm, as shown in *Figure 43*. After the rotor-shaft insertion was complete, the assembly was thoroughly inspected to ensure proper alignment, fit, and integrity of the rotor and shaft. This step ensured that the assembly met all tolerance requirements and was ready for the subsequent stages of the motor assembly process.

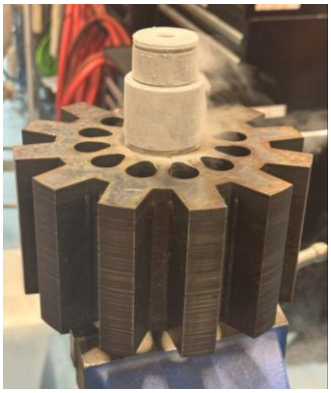

Figure 43 - Rotor Shaft Insertion

5.2.4 Completed Rotor Sub Assembly

The retaining rings and two KOYO 3NC6208ZZC3 shielded deep groove ball bearings were carefully installed on the rotor shaft assembly to complete the rotor subassembly, as shown in *Figure 44*. This critical step ensures that all components are securely attached and ready to operate.

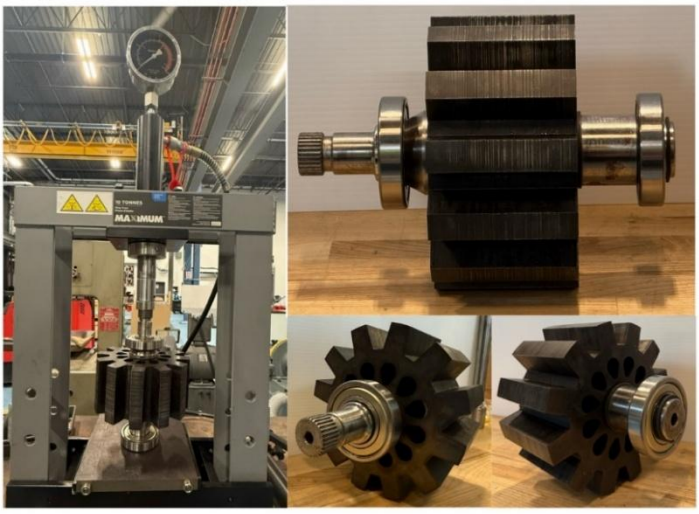

Figure 44 - Rotor Sub Assembly

The rotor shaft assembly without bearings was balanced to satisfy ISO Grade 2.5 criteria, as described by the ISO 21940-16 standard. This standard specifies the acceptable amounts of imbalance for spinning parts. ISO Grade 2.5 is specifically designed for high-speed rotors in electric motors, turbines, and precision machinery. This grade is especially significant for motors that operate at higher speeds, where low vibration and noise are critical for preserving performance and longevity [20]. *Table 12* shows the results after balancing the rotor.

Table 12- Rotor Balancing Results

Balance Tolerance

ISO Balance Grade	G 2.5
Iso Grade 2.5 (OZ. Inch)	0.175
Rotor Weight	35 LBS
Balance RPM	404
Operating Speed	3000

Original Reading	**Final Reading**
351° Left Angle	351° Left Angle
0.154 Left amount in OZ.	0.154 Left amount in OZ.
151° Right Angle	151° Right Angle
0.429 Right Amount in OZ.	0.429 Right Amount in OZ.

Balance Level

	Recommended	**Original**	**Final**
Left	0.088 OZ. Inch	0.308 OZ. Inch	0.0776 OZ. Inch
Right	0.088 OZ. Inch	0.857 OZ. Inch	0.0462 OZ. Inch
Total	0.175 OZ. Inch	1.165 OZ. Inch	0.1238 OZ. Inch

Final ISO Balancing Grade – G 1.76

5.3 Stator Sub Assembly

Several critical procedures must be completed precisely during the stator assembly process. The initial step is to prepare and install insulation within the stator slots. Nomex paper of 0.25 mm thickness is used as insulation between the coil windings and the stator to avoid short circuits. The Nomex paper is cut to fit the stator slots and carefully inserted, as shown in *Figure 45 (a)*. This insulation phase ensures electrical separation and guards against potential issues during operation. Following insulation, the coil windings are inserted into the stator slots. After the windings are correctly positioned, manufactured slot wedges are placed to retain the coils, as shown in *Figure 45 (b).* The slot wedges keep the windings aligned and stable under working conditions, preventing movement or displacement during motor operation. Heat sleeves and shrink tubing are added to the coil wires to provide extra insulation and protection, as illustrated in *Figure 45 (c)*. This procedure protects the wiring from electrical failures or damage while maintaining the stator assembly's durability and reliability.

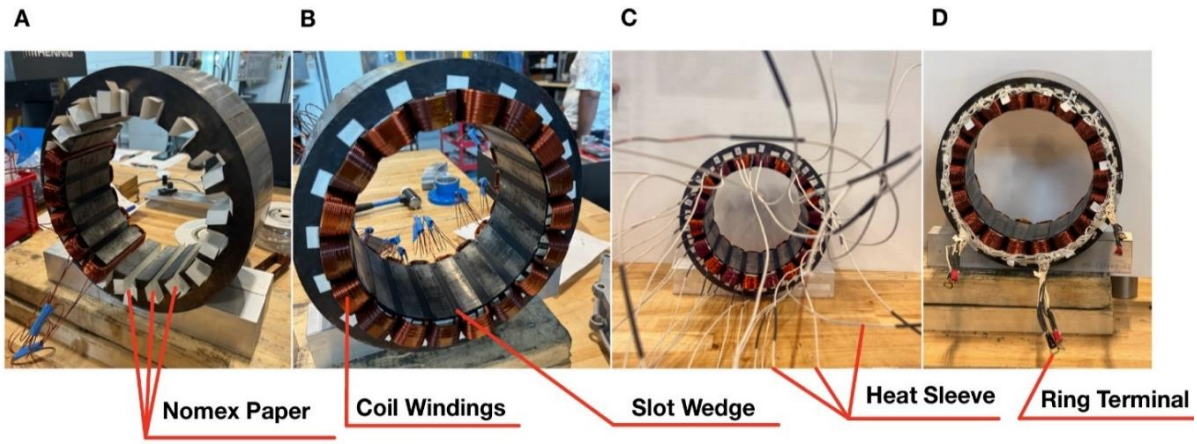

Figure 45 - Stator Assembly Process

The next step is to complete the stator's phase wiring. *Figure 46* depicts a phase and wiring diagram tailored explicitly for this motor. In SRM phase wiring, the positive (++ phase) and negative (-- phase) connections of each phase are retained together in the stator coil windings. This arrangement reduces the loop area of the phase current, decreasing magnetic interference and stray inductance that could result from separate current flows. Ensuring that each phase's positive and negative contacts are closely matched. NTC thermistors were installed in one of the coils of each phase total of three thermistors to monitor the temperature of the coil windings. These thermistors were carefully positioned and wired to ensure accurate temperature measurements without interfering with the motor's operation. This setup allows for real-time monitoring of coil temperatures, which provides critical data for evaluating the motor's thermal performance and ensuring safe operation.

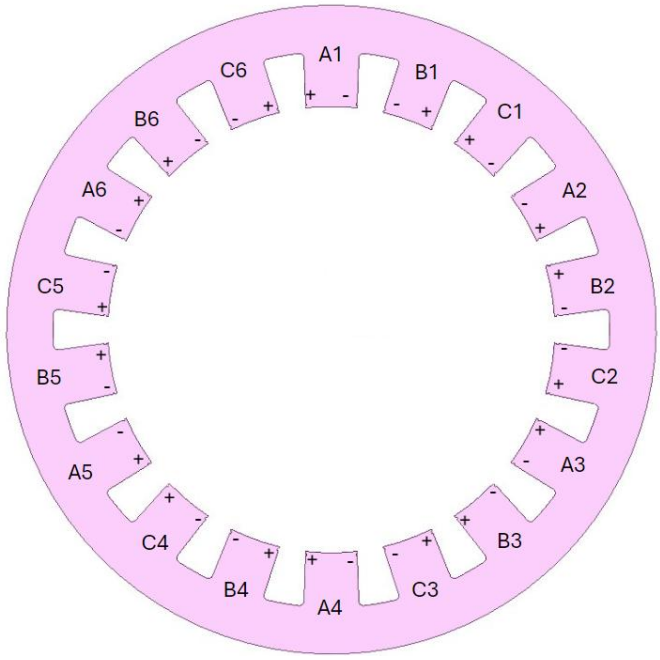

Figure 46 - Stator Phase Diagram

Finally, both positive and negative ring terminals are connected to each phase connection. These connectors allow for dependable integration of the stator with the motor's electrical system.

5.3.1 Challenges in Stator Assembly Testing

Three critical electrical tests were performed to ensure the assembled stator's reliability: a high-potential (Hipot) test to verify insulation integrity, a polarization index (PI) test to measure phase resistance, and a surge test to detect short circuits between phases. All three phases failed the high-potential test during initial testing, with arcs at 1120V, 1200V, and 1140V. All lacing and wiring had to be removed to locate the source of this failure. Each coil was tested individually, and three of the coils failed the high-potential test, arcing at 560V, 420V, and 480V. Further inspection

revealed microscopic damage to the insulation on these coils, as illustrated in *Figure 47*. The damage was attributed to problems with the coil insertion process and improper handling. New coils were wound and replaced in the stator assembly to solve this issue. After reassembly, the stator underwent the same tests.

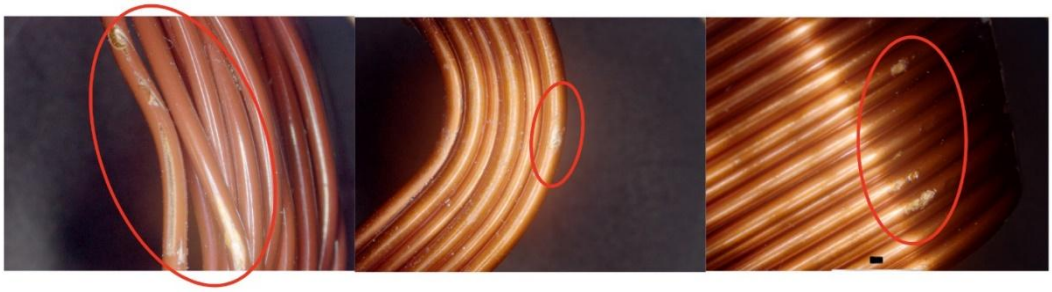

Figure 47 - Microscopic Damage to Insulation

After replacing the damaged coils, all three phases failed the high-potential test again. The lacing and wiring were again removed to inspect the stator. This time, it was discovered that the stator's end teeth lacked adequate insulation between the stator and coils, considering that the encapsulation is not applied yet. The lack of insulation allowed for electrical short circuit during the testing process. Additional insulation was applied to all end turns and coils, to address this issue, ensuring that the stator and windings were sufficiently separated. After insulating the end turns and reassembling the stator, all the wiring process was completed, and the assembly was ready for testing.

5.3.2 Stator Assembly Test Setup and Results

The stator was again retested using the Megger Baker DX diagnostic tool to verify its functionality. *Figure 48* shows the stator installed in a steel fixture connected to the ground for grounding. The tests with the Megger Baker DX provided detailed information on the stator assembly's insulation resistance (IR), phase resistance, and the performance of each phase.

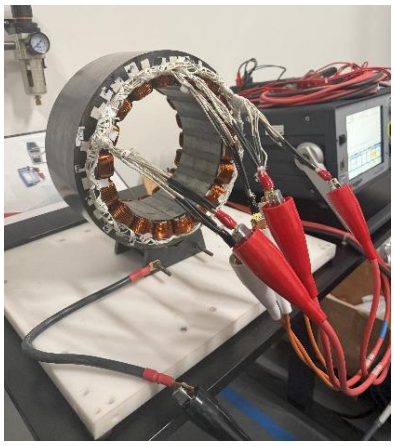

Figure 48 - Stator Assembly Testing

Phase resistance was tested and compared to the design parameters [7], and *Table 13* shows the results.

Table 13 - Phase Resistance Results

	Phase resistance @ 25°C Design Parameter	Phase resistance @ 25°C Experimental Validation
Phase A	**66.3142 mΩ**	**71.52 mΩ**
Phase B	**66.3142 mΩ**	**72.45 mΩ**
Phase C	**66.3142 mΩ**	**72.15 mΩ**

A Polarization index test was performed on the motor to evaluate IR at its maximum working voltage of 450V. The test lasted 10 minutes, allowing enough time for the insulation material's polarization effects to stabilize. This prolonged test duration ensures the IR is accurately assessed by considering the insulating materials' time-dependent behaviour. The Hipot test results are shown in F*igure 49* and *50*.

IR Results

Voltage [V]	I [µA]	IR [MΩ]
460	0.042	10952

DA/PI Results

Voltage [V]	DA Ratio	PI Ratio
460	1.5	1.7

HiPot Result

Voltage [V]	I [µA]	IR [MΩ]
1220	0.106	11509

DA/PI Results

Time [Minute(s)]	Voltage [V]	I [µA]	IR [MΩ]
00:15	460	0.059	7796.61
00:30	460	0.051	9019.61
00:45	460	0.045	10222.22
01:00	460	0.042	10952.38
01:30	460	0.039	11794.87
02:00	460	0.037	12432.43
02:30	460	0.034	13529.41
03:00	460	0.034	13529.41
04:00	460	0.032	14375.00
05:00	460	0.029	15862.07
06:00	460	0.028	16428.57
07:00	460	0.027	17037.04
08:00	460	0.025	18400.00
09:00	460	0.025	18400.00
10:00	460	0.024	19166.67

Figure 49- Polarization Index Test Result

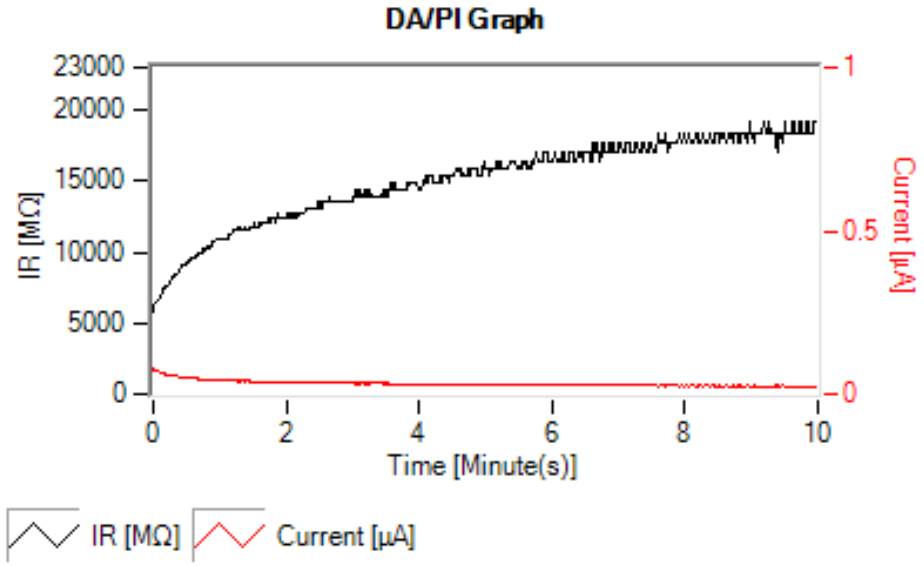

Figure 50 – Polarization Index Test Result Graph

In addition, the test voltage was gradually increased to 1200V to ensure that the insulation of the coils is adequate before the encapsulation.

End of Step Values

Step	Voltage [V]	I [µA]	IR [MΩ]
1	300	0.010	30000
2	630	0.043	14651
3	930	0.073	12740

Figure 51 –Step Voltage Test Results

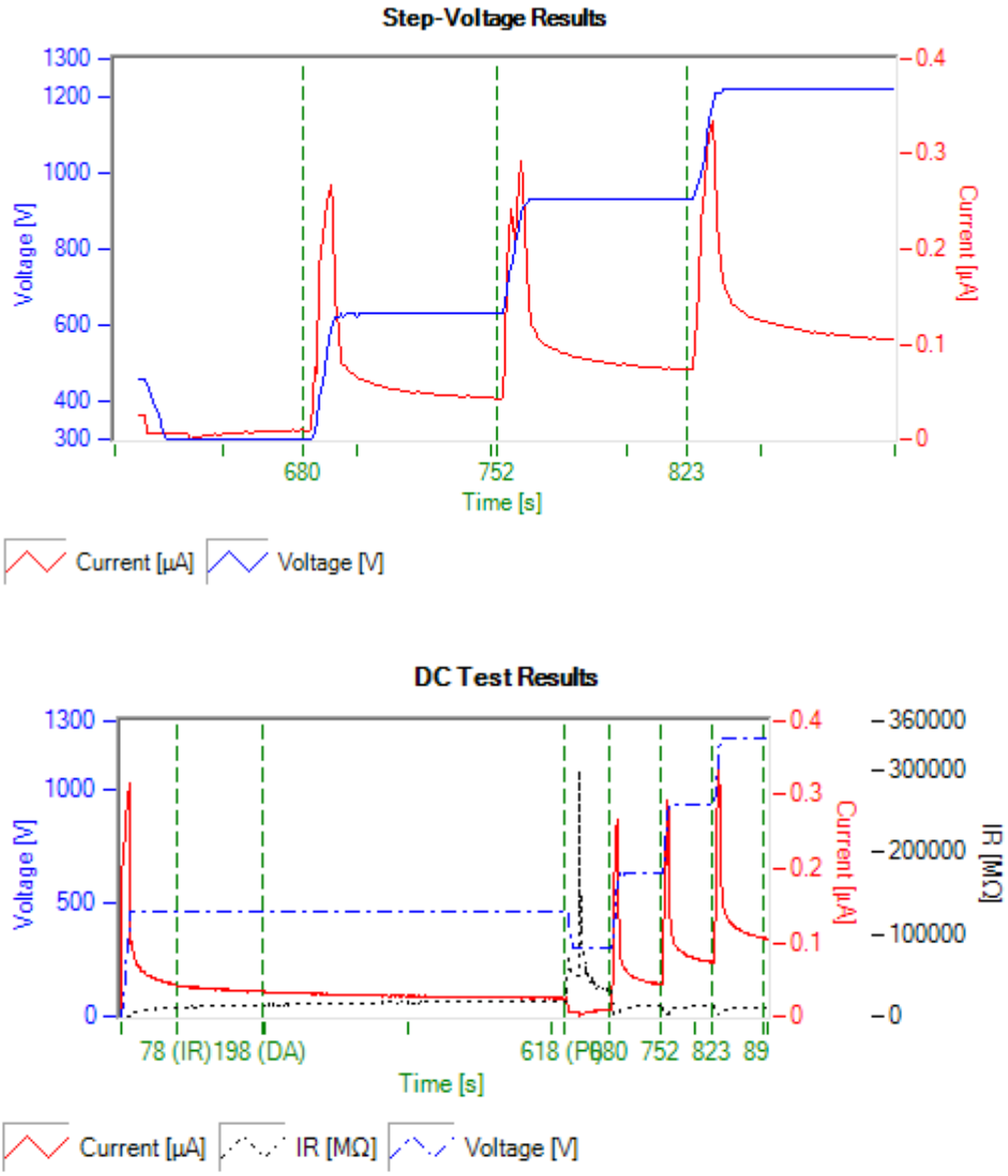

Figure 52 –Step Voltage Test Results Graph

Following the polarization index and step voltage test, the Surge test was performed on the motor at a peak voltage of 1200V to detect any short circuits between the three phases and determine performance consistency. This test is critical for detecting

phase-to-phase insulation flaws or variations in electrical properties that may affect the motor's operation. By applying high-voltage pulses, the test effectively simulates real-world electrical stresses, allowing for a thorough assessment of phase insulation, the detection of any discrepancies or defects, and uniform performance.

The results of the surge test are as follows:

Compare	Peak Voltage [V]	Number of Pulses	LL EAR Status	L-L EAR [%]
1-2	1230	10	PASS	1
2-3	1220	11	PASS	2
3-1	1210	10	PASS	2

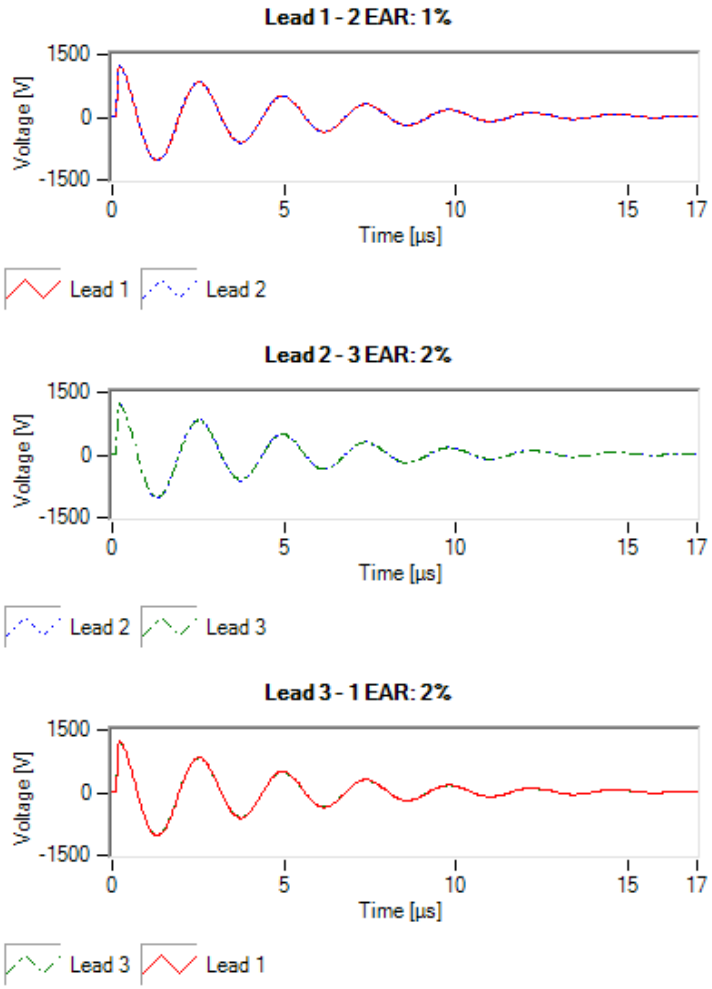

Figure 53 - Surge Test Results

Lead	Peak Voltage [V]	Number of Pulses	PP EAR Status	Max P-P EAR [%]
1	1230	10	PASS	2
2	1220	11	PASS	4
3	1210	10	PASS	3

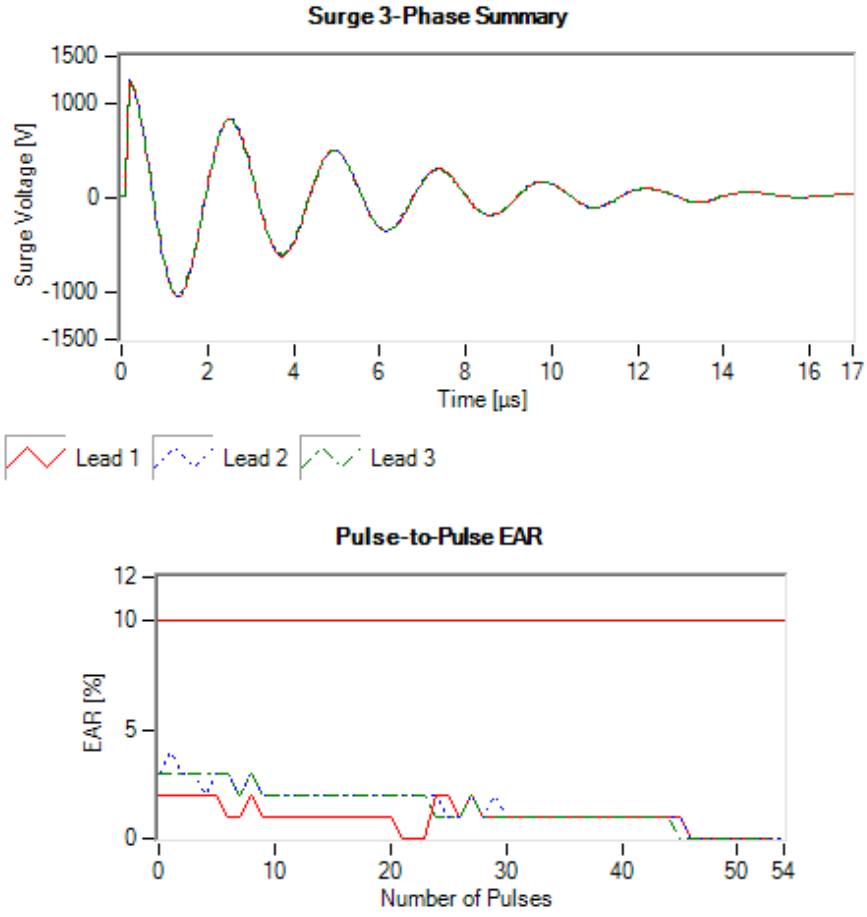

Figure 54 - 3 Phase Surge Test Results Summary

The Error Area Ratio (EAR) is a useful diagnostic metric in surge testing. It is used to detect winding faults, ensure electrical integrity, and check phase-to-phase consistency in motors. An EAR near zero indicates that the tested winding closely matches the reference, implying good condition. Peak-to-Peak EAR measures the difference between the peak amplitudes of waveforms from a tested winding and a reference waveform.

5.4 Full Motor Assembly

The results of the assembly tests show that all sub-assemblies were successfully completed. This section focuses on the motor's final assembly, which involves combining these three sub-assemblies to create a fully functional motor. The final assembly process is critical for ensuring that the individual components work together as an entire system.

5.4.1 Housing and Stator Assembly

The housing and stator subassemblies must be assembled to ensure that the radial and axial tolerances are met for the motor. The inner diameter of the housing where the stator sits is 280.0011 mm, while the stator's outer diameter is 280.1756 mm, resulting in an interference of 0.1745 mm. To ensure smooth assembly, the housing's thermal expansion was calculated to ensure the necessary clearance during the assembly process. By carefully heating the housing to achieve the necessary expansion, the stator was able to be inserted without exerting excessive force or risking damage to either component. The *Table 14* shows the thermal expansion calculation, and the temperature adjustments required to achieve the desired fit.

Table 14 - Inner Housing Thermal Expansion Calculation

Inner Housing (Inner Diameter)
Material -A356 T6 Aluminum
Initial Diameter (mm)= 280.0011mm
CTE=21.4 $X10^{-6}$
T1(°C) = 25°C
T2(°C) = 140°C
ΔT(°C) = 115°C
ΔD= 280.0011 X 0.0000214 X 115
ΔD(mm)= 0.6826mm
Final Diameter(mm)= 280.6837mm

After calculating the required thermal expansion, which resulted in an increased inner diameter of housing to 280.6837 mm, the stator was carefully aligned with the housing to ensure a proper fit. Figure 55 shows the assembled stator and housing, demonstrating the successful integration.

Figure 55 - Assembled Housing and Stator

5.4.2 Stator Encapsulation

Stator encapsulation coats the stator subassembly with epoxy resin, chosen for its excellent electrical insulating and thermal conductive properties. Encapsulation provides multiple benefits, including mechanical protection, electrical insulation, and efficient thermal management for stator components. *Figure 56* shows the coil's cross-section take under microscope, showing how the epoxy coats the windings to enhance insulation and thermal control. The epoxy effectively transfers heat from the coil during operation while improving the electrical insulation.

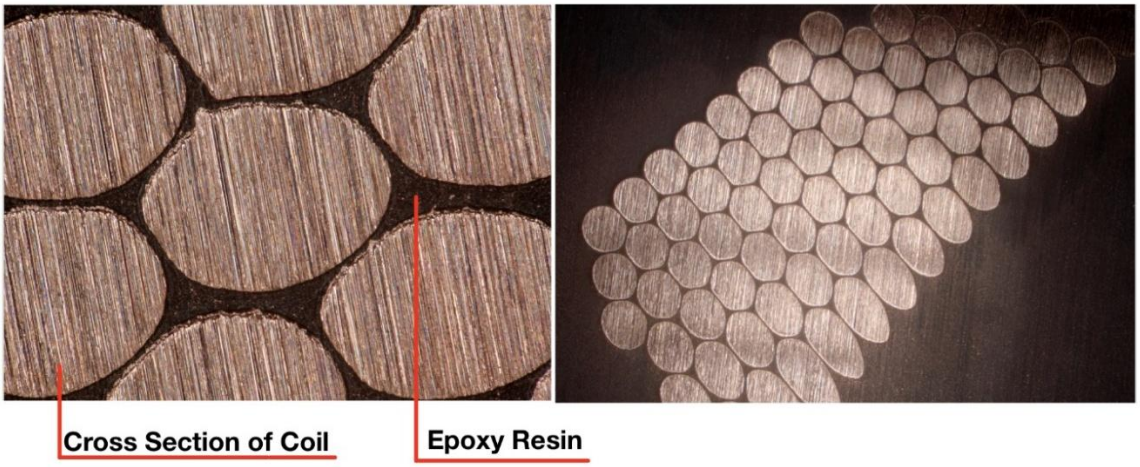

Figure 56 - Cross-Section of Coils After Encapsulation

This process used ultra-high molecular weight (UHMW) material as the centre potting tool with a compressive yield strength of 21Mpa. This material was chosen due to its superior machinability and material properties. The potting tool was designed to fit through the air gap between the stator without interfering. During encapsulation, the potting tool's thermal expansion was considered to ensure it adequately filled the air gap, preventing epoxy resin from flowing into this critical area. This was accomplished by analyzing the potting tool's thermal expansion properties. As the tool expands due to heat, it closes the air gap, effectively containing the epoxy within the stator windings. The base fixture for the potting tool was designed to fit with a 0.025 mm clearance, allowing for a simple and precise fit during assembly. Thermal expansion calculations for the potting tool and stator are shown in *Table 15.*

Table 15 - Thermal Expansion Calculation for Stator Encapsulation Process

Potting Tool	**Stator (Outer Diameter**
Material -UHMW Initial Diameter (mm)= 192.45mm CTE=19.8 $X10^{-5}$ T1(°C) = 25°C T2(°C) = 70°C ΔT(°C) = 45°C ΔD= 192.45X 0.000198 X 45 **ΔD(mm)= 1.714mm**	Material – HIPERCO® 50A Initial Diameter (mm) = 192.856mm CTE=9.59 $X10^{-6}$ T1(°C) = 25°C T2(°C) = 70°C ΔT(°C) = 45°C ΔD= 192.856X 0.00000959 X 45 **ΔD(mm)= 0.0832 mm**
Final Diameter(mm)= 194.164mm	**Final Diameter(mm)= 192.939mm**

Furthermore, FEA was used to validate the thermal expansion and determine stresses of the potting tool during the encapsulation process. *Figures 57A* and *57B* illustrate the radial displacement of the stator and potting tool under free-free conditions at 70^0C. It reveals a radial displacement of 0.064 mm in the stator and 0.91 mm in the potting tool. *Figure 57C* further depicts the radial displacement during the potting condition at 70^0C, highlighting the interaction between the components. *Figure 57D* depicts the linear stress distribution on the potting tool at 70^0C, with stress levels reaching up to 21 MPa in certain areas, which ensures the material stays within its

structural limits. This analysis ensures that the potting tool works well during encapsulation.

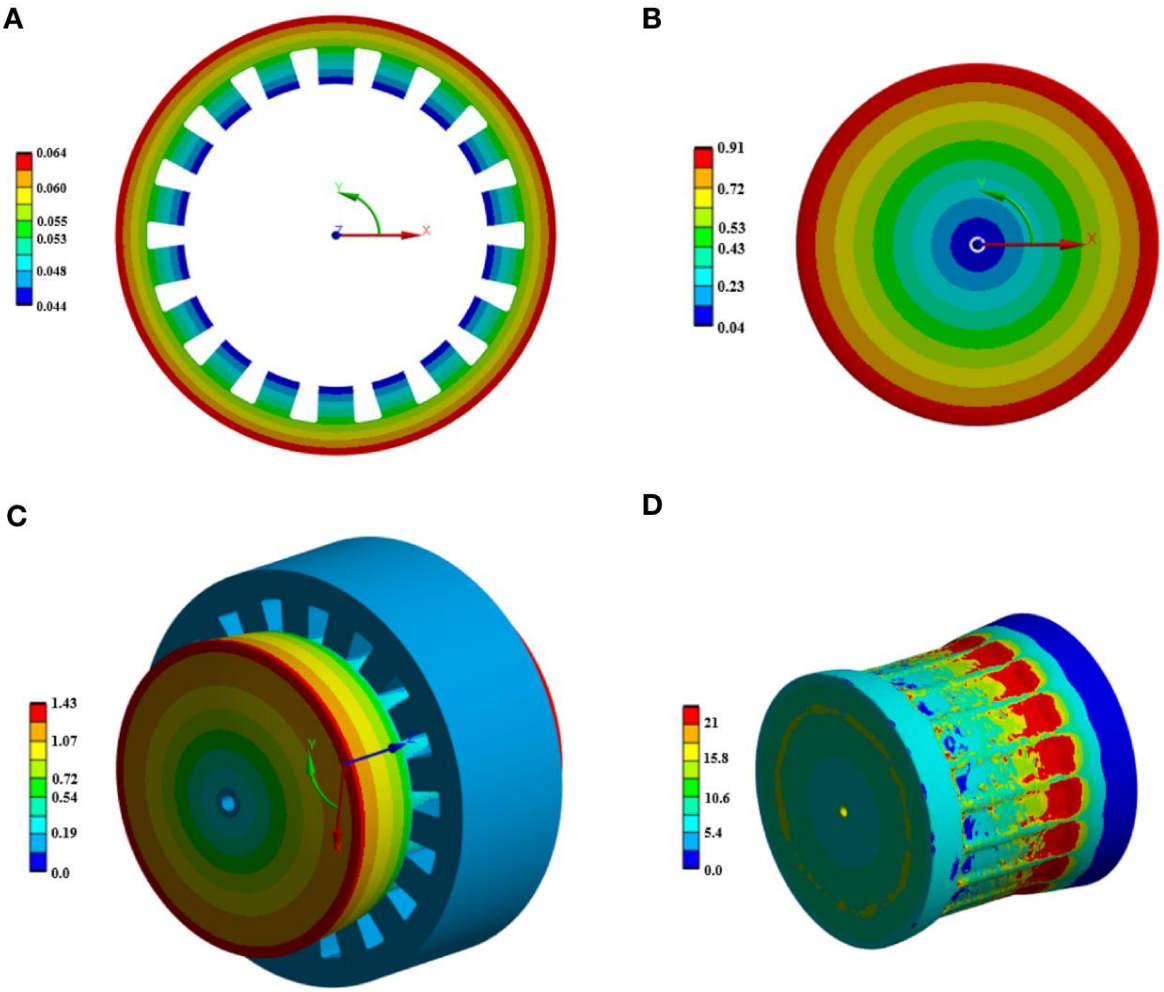

Figure 57 - FEA results for Stator and Potting Tool

Based on the calculations and analysis, the encapsulation fixture, shown in *Figure 58*, was designed to meet the specific requirements of the stator encapsulation process. This fixture holds the stator wiring securely in place during encapsulation, ensuring proper alignment and positioning.

Figure 58 - Design of Stator Encapsulation Fixture

The epoxy used for stator encapsulation is EFI 11T206 – 20290 / 7H013 – 50021. It was chosen because of its moderate mixed viscosity and long gel time, making it appropriate for high-speed production and manual application. This epoxy has low shrinkage and exothermic properties, reducing stress on the encapsulated components during curing. The material's thermal conductivity of 0.66 W/m·K makes it suitable for thermal management. The encapsulation fixture was designed and manufactured, then assembled with the stator to prepare for the encapsulation process. It was mixed and heated to 70°C before application to improve the epoxy's flow properties. The motor and assembled fixture were also heated to 70°C to improve the epoxy's flow and ensure that it was evenly distributed throughout the stator, including around the windings and insulation. *Figure 59* depicts the stator encapsulation process, including the fixture integration and epoxy application. This method ensures consistent and high-quality encapsulation.

Figure 59 - Stator Encapsulation Process

Following encapsulation, the motor was cured in an oven at 70°C for 3 hours to allow the epoxy to set fully. After curing, the motor was removed from the oven and cooled for 24 hours. This cooling period ensured that the potting tool fixture returned to its original shape, allowing it to be removed safely and meticulously without damaging the stator or encapsulated components. This step was critical to ensuring the encapsulation's integrity as it confirmed that the epoxy had fully hardened and adhered to the stator while keeping the windings precisely aligned and insulated. *Figure 60* depicts the completed encapsulation process, with the stator coated in fully cured epoxy and ready for the next stage of motor assembly.

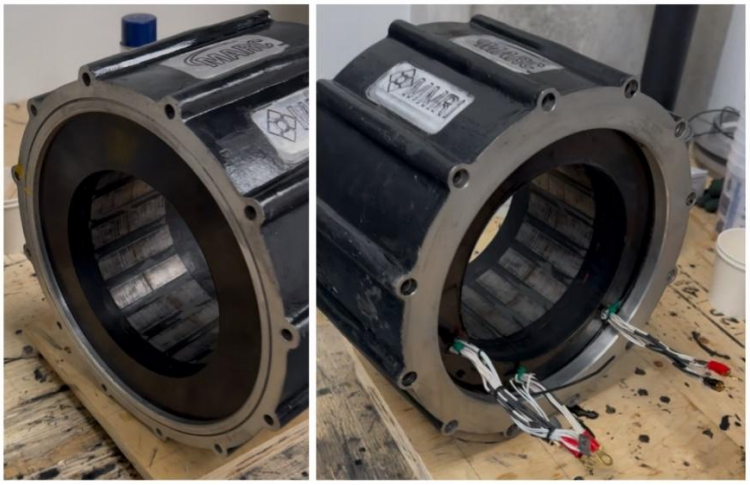

Figure 60 - Completed Stator Encapsulation

After the stator encapsulation process, a series of tests, including polarization index (PI), step voltage, Hipot, and surge tests, were repeated to evaluate the impact of encapsulation on the insulation resistance (IR) and PI ratio. The PI test is a critical diagnostic tool used to assess the condition of the stator winding insulation. It measures the ratio of insulation resistance at the 10-minute mark to that at the 1-minute mark. As detailed in Section 5.3.2 and *Figure 49*, the PI ratio before encapsulation was 1.7, with a 1-minute IR value of 10,952 MΩ and a 10-minute IR value of 19,166 MΩ. After encapsulation, the PI ratio increased significantly to 9, with the 1-minute IR value rising to 51,111 MΩ and the 10-minute IR value reaching 459,999 MΩ, as shown in *Figure 61*. This substantial improvement in the PI ratio demonstrates encapsulation's effectiveness in enhancing the stator windings' insulation resistance.

DA/PI Results

Voltage [V]	DA Ratio	PI Ratio
460	4.3	9

HiPot Result

Voltage [V]	I [µA]	IR [MΩ]	IR [MΩ] Corrected 40°C (Thermoplastic)
1910	0.022	86818	32221

DA/PI Results

Time [Minute(s)]	Voltage [V]	I [µA]	IR [MΩ]
00:15	460	0.022	20909.09
00:30	460	0.013	35384.61
00:45	460	0.010	46000.00
01:00	460	0.009	51111.11
01:30	460	0.006	76666.67
02:00	460	0.005	92000.00
02:30	460	0.004	114999.99
03:00	460	0.003	153333.33
04:00	460	0.002	229999.99
05:00	460	0.002	229999.99
06:00	460	0.002	229999.99
07:00	460	0.001	459999.98
08:00	460	0.002	229999.99
09:00	460	0.002	229999.99
10:00	460	0.001	459999.98

Figure 61- Encapsulated Stator Polarization Index Test Result

The step voltage and Hipot tests were conducted according to IEEE Standard 95-2002 [21], which specifies that the test voltage should be two times the machine's rated voltage plus 1,000 V. This standard ensures the insulation system's ability to

withstand potential voltage spikes. For this prototype, with a rated voltage (VDC) of 450 V, the calculated test voltage was 1,900 V. *Figures 62* and *63* show the results of the encapsulated stator, which demonstrate its ability to meet the required insulation standards.

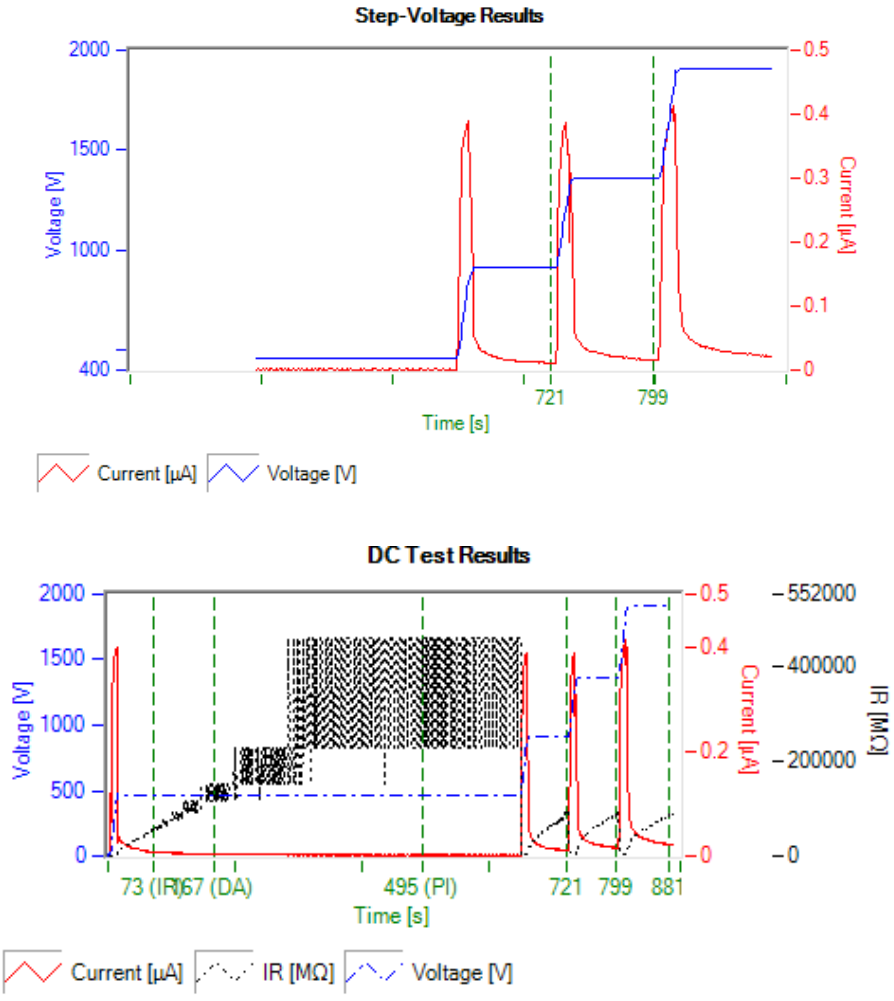

Figure 62 –Encapsulated Stator Step Voltage Test Results Graph

HiPot Result

Voltage [V]	I [µA]	IR [MΩ]	IR [MΩ] Corrected 40°C (Thermoplastic)
1910	0.022	86818	32221

Figure 63 –Encapsulated Stator Hipot Test Results

A surge test was conducted on the encapsulated stator, and the results are shown in *Figure 64*.

Compare	Peak Voltage [V]	Number of Pulses	LL EAR Status	L-L Limit 20 L-L EAR [%]
1-2	1910	10	PASS	1
2-3	1910	11	PASS	1
3-1	1910	11	PASS	1

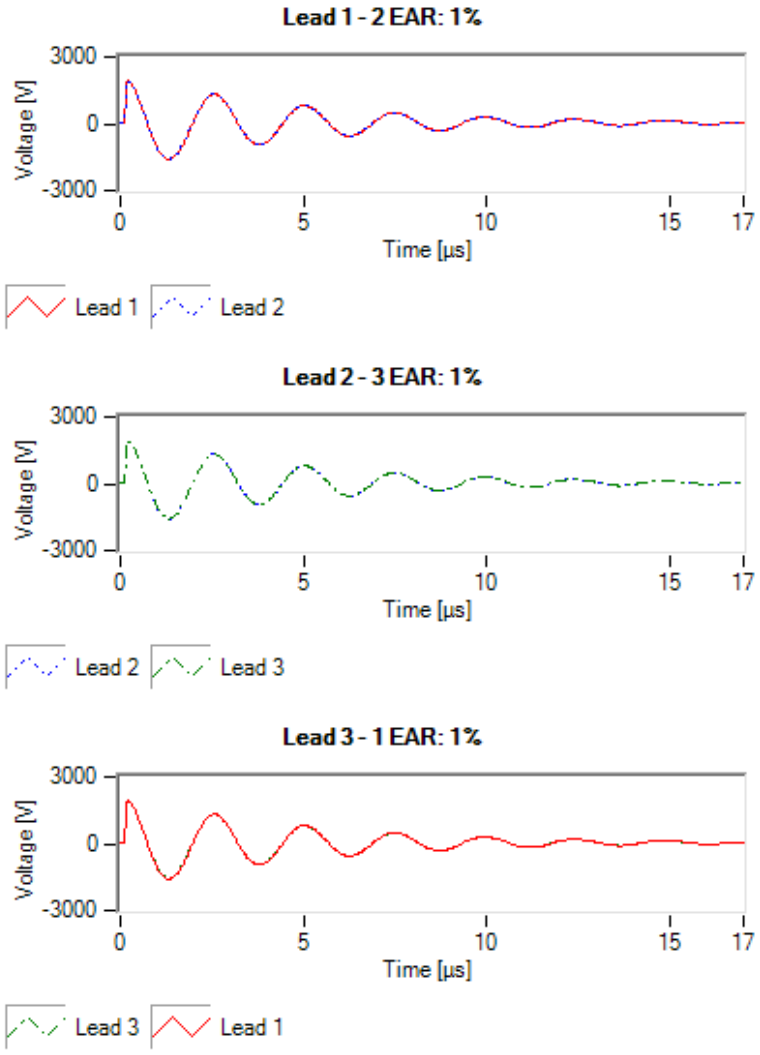

Figure 64 –Encapsulated Stator Surge Test Results

5.4.3 Rotor Subassembly Installation

Installing the rotor subassembly is the final and most crucial step in the motor assembly process. This step ensures that the rotor is correctly integrated with the housing and other components. The process began with installing End Cap A, which has a wave spring within the bearing hole. End Cap A was securely bolted, and the rotor subassembly was carefully inserted to ensure the bearings fit precisely into the bearing hole, as shown in *Figure 65*. Following the successful installation of the rotor subassembly, End Cap B was mounted while keeping the housing aligned and the motor's wiring properly routed and positioned. This meticulous assembly process ensures that the rotor and bearings are properly aligned and securely integrated into the motor housing.

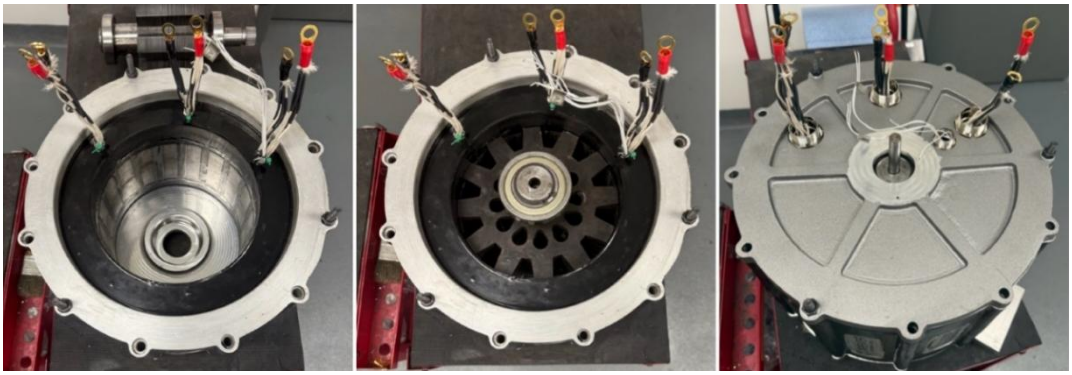

Figure 65 - Rotor Subassembly Installation

5.5 Weight of LSA SRM Components

Table 16 details the weight of each subassembly and the various stages of the motor's development. This breakdown highlights each component's contribution to the total motor weight.

Table 16 - Weight of Motor Components

Component	Weight	Motor Weight Contribution (%)
Housing Sub Assembly	18kg	27.66%
Rotor Sub Assembly	16.8kg	25.63%
Stator Sub Assembly after Encapsulation	28.6kg	43.91%
Fittings and other components	1.8kg	2.8%
Completed Motor with all Fittings	65.2kg	100%

5.6 Completed Prototype Development

The housings were bolted to a torque of 40 Nm to ensure assembly structure and keep the housings secure. All fittings, including wiring and coolant channels, were inspected, and sealed to ensure proper functionality and leak-free operation. This marked the end of the prototype SRM designed for light sport aircraft, as shown in

Figure 66. The final assembly shows how all components have been integrated to create a fully functional motor ready for testing and evaluation.

Figure 66 - Completed Prototype Development

5.7 Summary

The assembly and testing processes are designed to integrate components with high precision and ensure the prototype is operationally ready. This work emphasizes the rigorous assembly of subassemblies, such as the housing, rotor, and stator, focusing on thermal expansion and interference fit. Under various conditions, components were thoroughly tested for insulation integrity, phase resistance, and coolant performance. Experimental testing validated changes to manufacturing tolerances and thermal behaviors.

Chapter 6- Conclusions and Future Work

6.1 Conclusions

SRMs are ideal for electrified Light Sport Aircraft (LSA) propulsion systems due to their ability to effectively handle propeller load and low noise impact in an isolated cabin environment. Electric LSAs have numerous advantages over conventional LSAs, such as higher efficiency, smaller and lighter motors, improved aerodynamics, simpler or no gearboxes, and less complex cooling systems. Electric LSAs also emit no greenhouse gases, minimizing environmental impact while lowering operational and purchasing costs. The proposed direct-drive SRM in this study is intended to replace a 70-kW Permanent Magnet Synchronous Motor (PMSM) used in aerospace applications while maintaining the equivalent dimensional and operational constraints. The iron-cobalt alloy HIPERCO® 50A was chosen as the core material for this design due to its high magnetic saturation to increase torque density. The prototype shows the successful development of an SRM optimized for LSA applications, with a small air gap length of 0.4 mm. The small air gap, critical for motor efficiency, was maintained using strict tolerances achieved through advanced design, modelling, and precision manufacturing. Key components, such as the housing, rotor, stator, and shaft, were manufactured with high dimensional accuracy and addresses issues in the assembly process such as thermal expansion and interference fit. The project's stator encapsulation process was a significant focus, with epoxy resin used

to provide electrical insulation and thermal management. The encapsulation tooling was designed to ensure consistent epoxy application. Testing the components of subassemblies confirmed that the assembly processes were successfully completed. The final assembly successfully combined the rotor subassembly, stator, and housing, ensuring proper alignment and functionality. This study lays a solid foundation for further investigation of SRM technology in aviation, focusing on increasing efficiency and reliability for electrified light sport aircraft.

6.2 Future Work

The prototype developed for this thesis has several areas for improvement. To reduce post-processing requirements and increase production efficiency, high vacuum high-pressure die casting could be used for the housing subassembly. Improving the manufacturing techniques for the rotor and stator laminations would boost their quality and performance. An automated epoxy mixer and a vacuum chamber to remove air pockets during encapsulation would result in a more consistent and reliable insulation process. Further advancements could focus on increasing the design's scalability for mass production, lowering costs while maintaining high performance. The Ball bearings will face greater thrust and radial loads in the actual motor application. To handle these additional forces, the bearing configuration may need to be modified, with one of the two deep groove ball bearings replaced by a tapered roller bearing. This modification would ensure durability and resilience under the anticipated loads in the motor's intended operating environment. The

prototyped motor should undergo extensive electromagnetic tests, performance evaluations, validations, and calibrations to ensure it meets the design requirements.

References

[1] United Nations Framework Convention on Climate Change (UNFCC). (May. 2016) Methodological Issues under the Convention: Emissions from Fuel Used for International Aviation and Maritime Transport. [Online]. Available: https://www.icao.int.

[2] U.S. Department of Transportation and Transport Canada. (Feb. 2021) Government of Canada Joint Statement by Transport Canada and the U.S. Department of Transportation on the Nexus between Transportation and Climate Change. [Online]. Available: https://www.canada.ca/.

[3] David Suzuki Foundation on Nature. (Mar. 2020) Air Travel and Climate Change. [Online]. Available: https://davidsuzuki.org/.

[4] The U.S. Department of Energy Bioenergy Technologies Office (BETO). (Sept. 2021) Sustainable Aviation Fuels [Online]. Available: https://www.energy.gov/.

[5] UBS Investment Bank. (Jun. 2019) Green Power: Will climate change propel the sector towards Hybrid Electric Aviation. [Online]. Available: https://www.ubs.com/.

[6] M. Kozlova, T. Nykanen, and J Yeomans, “Technical advances in aviation electrification: enhancing strategic R&D investment analysis through simulation decomposition,” Sustainability, vol. 14, no. 1, p. 414, Dec. 2021.

[7] Abdollahi, Mohammad Ehsan (2022) “Design of a Switched Reluctance Motor for a Light Sport Aircraft Application” http://hdl.handle.net/11375/27753.

[8] J. Overton, "Fact Sheet: The Growth in Greenhouse Gas Emissions from Commercial Aviation," Environmental and Energy Study Institute, Oct. 2019. [Online]. Available: https://www.eesi.org/.

[9] Bilgin, Berker, James Weisheng Jiang, and Ali Emadi. "Switched reluctance motor drives: fundamentals to applications." Boca Raton, FL (2018).

[10] https://www.aerospacetestinginternational.com/features/how-rolls-royces-spirit-of-innovation-broke-the-electric-speed-record.html.

[11] Pipistrel Aircraft. E-811 EASA TC – Pipistrel Aircraft. (2020). Accessed: July. 16, 2024. [Online]. Available: https://www.pipistrel-aircraft.com

[12] MagniX Co. Powertrains., Accessed: July. 15, 2024. [Online]. Available: https://www.magnix.aero

[13] F. Anton, O. Otto, J. Hetz, and T. Olbrechts, "Presentation on behalf of Siemens eAircraft Siemens eAircraft Siemens Next47 Siemens Digital Factory PLM Software Simulation & Testing Solutions", 2018. Accessed: Sep. 28, 2022. [Online]. Available: https://www.ie-net.be

[14] "eFlyer 2 Prototype Begins New Flight Test Program with Siemens Production Motor", PF Product Finishing, Jul. 19, 2019. Accessed: July. 15, 2024. [Online]. Available: https://www.aviationpros.com/

[15] “HIPERCO® 50AData sheet CARPENTER ELECTRIFICATION” [Online]. Available: https://www.carpenterelectrification.com/

[16] Abdollahi, M.E.; Zahid, A.; Vaks, N.; Bilgin, B. Switched Reluctance Motor Design for a Light Sport Aircraft Application. Machines 2023, 11, 362. https://doi.org/10.3390/machines11030362

[17] “Material Property Datasheet AISI 8620 STEEL” [Online]. Available: https://www.matweb.com/search/datasheet.aspx?matguid=ddb18ff0327347ceb2cc59fc0d761295

[18] "University Physics Volume 2" https://openstax.org/books/university-physics-volume-2/pages/1-3-thermal-expansion

[19] "Aluminum A356.0-T6, Sand Cast" Available Online: https://www.matweb.com/search/datasheet_print.aspx?matguid=d524d6bf305c4ce99414cabd1c7ed070

[20] "Mechanical vibration — Rotor balancing" https://www.iso.org/standard/54074.html

[21] 95-2002, IEEE Recommended Practice for Insulation Testing of AC Electric Machinery (2300 V and Above) With High Direct Voltage, IEEE Standard, 2002.